2012

# A Study Of Biodegradable Ceramic Coatings For Magnesium-Based Implants

Erica L. Clinard
*North Carolina Agricultural and Technical State University*

# A STUDY OF BIODEGRADABLE CERAMIC COATINGS FOR MAGNESIUM-BASED IMPLANTS

by

Erica L. Clinard

A thesis submitted to the graduate faculty
in partial fulfillment of the requirements for the degree of
MASTER OF SCIENCE

Department: Mechanical Engineering
Major: Mechanical Engineering
Major Professor and Co-Advisor: Dr. Jagannathan Sankar
Advisor: Dr. Sergey Yarmolenko

North Carolina A&T State University
Greensboro, North Carolina
2012

School of Graduate Studies
North Carolina Agricultural and Technical State University

This is to certify that the Master's Thesis of

Erica L. Clinard

has met the thesis requirements of
North Carolina Agricultural and Technical State University

Greensboro, North Carolina
2012

Approved by:

| | |
|---|---|
| _____ | _____ |
| Dr. Jagannathan Sankar<br>Major Professor and Co-Advisor | Dr. Sergey Yarmolenko<br>Advisor |
| _____ | _____ |
| Dr. Jenora Waterman<br>Committee Member | Dr. Dhananjay Kumar<br>Committee Member |
| _____ | _____ |
| Dr. Devdas Pai<br>Committee Member | Dr. Samuel Owusu-Ofori<br>Department Chairperson |

_____
Dr. Sanjiv Sarin
Associate Vice Chancellor for Research
and Dean of Graduate Studies

# DEDICATION

For my family. Your guidance, love and support have got me to this point. Thank you!

# BIOGRAPHICAL SKETCH

Erica L. Clinard was born in Winston-Salem, North Carolina. She received a Bachelor of Science degree in Mechanical Engineering from the University of North Carolina at Charlotte in December 2010. As an undergraduate student, Erica worked as a teaching assistant for the Lee College of Engineering, a supplemental instructor of chemistry for the University Center for Academic Excellence and a resident assistant for Housing and Residence Life. She joined Delta Zeta sorority and volunteered as a campus tour guide. Erica joined the Master of Science program in Mechanical Engineering at North Carolina Agricultural and Technical State University in January 2011. She worked as a teaching assistant in the Department of Mechanical Engineering during the spring semester of the 2010-2011 academic year and as a research assistant for the National Science Foundation Engineering Research Center for Revolutionizing Metallic Biomaterials from the summer of 2011 until the completion of her degree requirements.

# ACKNOWLEDGMENTS

To Dr. Jagannathan Sankar, thank you for giving me the opportunity to work on a research area involved within the Engineering Research Center. This opportunity has allowed me the opportunity to learn new skills as well as meet an outstanding group of people. I have learned so much outside of my research topic due to the abilities of those that are a part of the ERC team. I am proud to say that I was a part of the ERC and all of the work that is being accomplished.

To Dr. Sergey Yarmolenko, I thank you for all of your guidance and knowledge. I thank you for taking on the responsibility of being my advisor. I am amazed at how much I have learned from you and how much of that knowledge I will be able to apply to everyday life.

To Dr. Jenora Waterman, I thank you for all of your patience as I attempted to learn the necessary information to complete the biological assays needed for my research. I appreciate the answers to all of my many questions and the time you spent to help me design my experiments.

To Dr. Dhananjay Kumar, thank you for your advice and help as I entered A&T and for welcoming me into the ERC.

To Dr. Pai, thank you for looking over my thesis and providing comments on how to improve it.

To Dr. Zhigang Xu, thank you for your help with the SEM. Your guidance and patience while teaching me how to use the SEM allowed me to learn the skills necessary to use an SEM in the future.

To Dr. Ram Gupta, I appreciate all of your help with the XRD machine. I know that I still have a lot to learn about that machine but believe that your help has provided me with the basic knowledge needed to use an XRD in the future.

To Ms. Dawn Conklin, thank you for your many hours of help while I completed my biological assays. Your willingness to stay late while I completed my assays did not go unnoticed and I thank you for being willing to stay around just in case I had a question.

To Mr. Ruben Kotoka, it is because of all your hard work and help that I am graduating. Thank you for being willing to help me with anything, for answering my questions, for showing me how to do everything I had to do in order to complete my research and for editing the first draft of my thesis; I know it was a tough job. THANK YOU!

To Ms. Svitlana Fialkova, thank you for helping me with the AFM measurements as well as going through the editing process with me. I would have been completely lost without your expert help! Thank you!

To my lab mates, Mr. Leon White, Ms. Nevija Watson, Ms. Lauren Douglas-Byrd, Mr. Daniel Owuor, Mr. Christopher Smith, and Mr. Christopher Mahoney, thank you for all of the laughs and good times; our Friday lunch dates will be missed! Thank you for all that you have done. I wish you all luck in your future endeavors. Thank you Leon for answering ALL of my questions!

# TABLE OF CONTENTS

# LIST OF FIGURES

**FIGURE** **PAGE**

# LIST OF TABLES

**TABLE** **PAGE**

# NOMENCLATURE AND SYMBOLS

| | |
|---|---|
| AFM | Atomic Force Microscopy |
| Al | Aluminum |
| $Al_2O_3$ | Aluminum Oxide |
| AlMn | Aluminum Manganese |
| AlN | Aluminum Nitride |
| Ar | Argon |
| BSE | Back Scattered Electrons |
| $Cl^-$ | Chloride Ion |
| Co-Cr | Cobalt Chromium |
| DC | Direct Current |
| DI | DeIonized |
| DMEM | Dulbecco's Modified Eagle Medium |
| EthD-1 | Ethidium Homodimer-1 |
| FBS | Fetal Bovine Serum |
| $Fe_2O_3$ | Ferrous Oxide |
| FeO | Ferric Oxide |
| $H_2O$ | Water |
| HA | Hydroxyapatite |
| HCl | Hydrochloric Acid |
| IGSCC | Intergranular Stress Corrosion Cracking |
| MgO | Magnesium Oxide |

| | |
|---|---|
| $Mg(OH)_2$ | Magnesium Hydroxide |
| NaBr | Sodium Bromide |
| NaCl | Sodium Chloride |
| NaOH | Sodium Hydroxide |
| NCAT | North Carolina Agricultural and Technical State University |
| $O_2$ | Oxygen |
| PBS | Phosphate Buffered Saline |
| PDC | Pulsed Direct Current |
| PPB | Parts Per Billion |
| RF | Radio Frequency |
| RGA | Residual Gas Analyzer |
| SCC | Stress Corrosion Cracking |
| sccm | Standard Cubic Centimeter per Minute |
| SE | Secondary Electrons |
| SEM | Scanning Electron Microscopy |
| TGSCC | Transgranular Stress Corrosion Cracking |
| TiN | Titanium Nitride |
| XRD | X-Ray Diffraction |

# ABSTRACT

**Clinard, Erica L.** A STUDY OF BIODEGRADABLE CERAMIC COATINGS FOR MAGNESIUM-BASED IMPLANTS. (**Advisor: Dr. Sergey Yarmolenko; Co-Advisor: Dr. Jagannathan Sankar),** North Carolina Agricultural and Technical State University.

Magnesium and its alloys are being used as biodegradable implants due to their similarity to natural bone. Functional coatings applied to magnesium-based implants provide protection from corrosion, promote osteointegration and improve the overall biocompatibility of the implant. However, an intermediate layer is needed between the functional coating and implant to serve as a galvanic barrier and slow the rate of corrosion of the implant. The objective of this study is develop some understanding of biodegradable, ceramic coatings that control the rate of corrosion of a magnesium-based implant by: optimizing parameters for fabricating metal oxides, determining surface roughness parameters, determining dependence of resorption time on coating thickness and determining the biological compatibility of aluminum oxide, ferric oxide and zinc oxide.

Magnetron sputtering has been used to manufacture high quality ceramic coatings through pulsed direct current sputtering technique. Aluminum oxide, zinc oxide and iron oxide were characterized by an optical density method, x-ray diffraction, scanning electron microscopy and atomic force microscopy. From this study, it was determined that: 1) magnetron sputtering can produce high quality, metal oxide films, 2) an optical density method can be used to obtain resorption rates of aluminum oxide coating and 3) aluminum oxide, iron oxide and zinc oxide exhibit promising biocompatibility based

upon results from adhesion and LIVE/DEAD cell viability assays. Aluminum oxide, ferric oxide and zinc oxide would serve as good biocompatible, galvanic separators and would control the rate of corrosion of a magnesium-based implant. Using ceramic materials as intermediate layers between magnesium-based implants and functional metallic coatings has the ability to create many applications for the use of magnesium implants.

# CHAPTER 1

# INTRODUCTION

## 1.1 Background

Within their lifetime, the average person will break two bones (Karriem-Norwood 2012). Along with the possibility of breaking a bone, the ligaments around these bones can be injured. Injuries of the anterior cruciate ligament (ACL), located in the knee, are thought to occur as frequently as 1 in 3,000 people. Each year, it is estimated that over 100,000 ACL reconstructions are performed in addition to an estimated 22,000 knee revision operations. While the ACL is just a single part of the knee, sometimes the entire knee must be replaced. In 2010, the cost of a total knee arthroplasty was approximated at $73,696. Although ACL reconstruction surgery has a success rate of 80-90%, those patients that have the 20% of surgeries that are unsuccessful must undergo additional surgeries that are costly, risky and can be painful. One additional surgery includes a knee scope to remove the old screws or other fixation devices (Southern California Orthopedic Institute 2012).

## 1.2 Problem Statement

Current metal implants are developed from titanium, stainless steel, a cobalt-chromium (Co-Cr) alloy, etc. Although these implants have been found effective, they are permanent once implanted and have been associated with many medical issues. Upon implantation, the risk of local inflammatory reactions along with lesions including soft tissue masses and tissue necrosis is too great. These metal implants cannot be implanted into patients with known moderate to severe renal insufficiency, patients with suppressed

immune systems and females of childbearing age (FDA 2012). Those patients that cannot accept a permanent metal implant need an alternative. The development of a biodegradable metal implant would offer these patients a solution. A biodegradable metal implant would provide the strength required of an implant without the harmful side effects. A biodegradable implant could be coated with a functional coating such as silver (Au) that is known for its antibacterial properties, which could be used in patients with suppressed immune systems to help fight infections. Another advantage of a biodegradable implant is that once implanted, the implant will gradually degrade as the bone reconstructs itself. Magnesium is a good material choice to develop as an implant because it is an essential element needed in the body and any excess can be excreted easily.

Magnesium, however, corrodes at a rate much faster than the rate of bone regrowth. If a magnesium implant is coated with a functional coating, the magnesium with corrode even faster than normal due to galvanic corrosion. To control the rate of corrosion as well as prevent galvanic corrosion between magnesium and a functional coating, an intermediate layer should be developed. Figure 1.1 models the significance of the development of a functional ceramic coating. Figure 1.1a depicts magnesium and a functional coating. Once submerged, the solution can enter through the pores of the functional coating and the magnesium begins to corrode at a high rate. Figure 1.1b shows the intermediate ceramic coating. Although the ceramic coating also contains pores, the amount compared to that of the functional coating is minimal. If the pores of the ceramic

coating lay under the functional coating, magnesium will be shielded from corrosion. Some corrosion will occur, but it will be at a slow controlled rate.

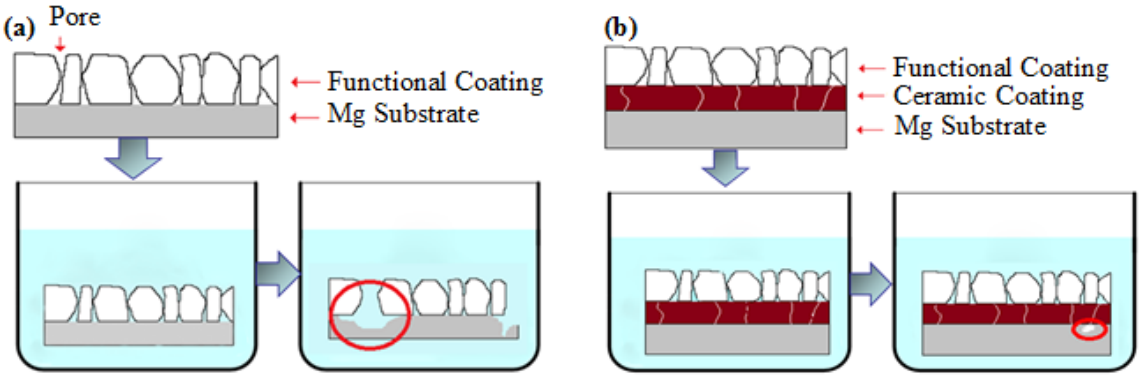


**Figure 1.1. (a) Magnesium and a functional coating. (b) Magnesium and functional coating separated by an intermediate layer.**

For the development of the intermediate ceramic coating, it was important to focus on materials that will be interacting with bone cells, or osteoblasts. Materials for bone tissue engineering should have a combination of properties, which include osteoinductive property, osteoconductive property and osteointegration property. A material that has an osteoinductive property is capable of promoting the differentiation of progenitor cells down an osteoblastic lineage. An osteoconductive property is one that supports bone growth and encourages the ingrowth of surrounding bone, while an osteointegration property integrates into surrounding bone (Basu, Saha et al. 2010).

### 1.3 Objectives

The goal of this study is to develop some understanding of biodegradable, ceramic coatings that will control the rate of corrosion of a biodegradable metallic implant by:

i. optimizing parameters for manufacturing high quality metal oxide (ceramic) coatings using a reactive sputtering process,

ii. determining surface roughness through the use of scanning electron microscopy (SEM) and atomic force microscopy (AFM)

iii. determining dependence of the resorption time of ceramic coatings based on coating thickness and

iv. determining the biological compatibility of the ceramic coatings: aluminum oxide ($Al_2O_3$), ferric oxide ($Fe_2O_3$) and zinc oxide (ZnO).

# CHAPTER 2

# LITERATURE REVIEW

## 2.1 Biomaterials

### *2.1.1 Introduction*

A biomaterial is any material, natural or synthetic, that comprises the whole or part of a living structure or a biomedical device which performs, augments, or replaces a function that has been lost through disease or injury (Sharma, Sehgal et al. 2003; Chim and Gosain 2009; Hazer, Kılıçay et al. 2012). Biomaterials have been used in history dating back to 600 AD when the Mayans used seashells shaped as teeth as dental implants (Gradwell 2010). As advancements in medicine were made, it was found that certain types of materials would succeed in the harsh environment of the body.

### *2.1.2 Metals*

#### *2.1.2.1 Introduction*

Metals are crystalline solids that are composed of elemental, positively charged ions in a cloud of electrons. The physical properties of metals include: luster (shininess), good conductors of heat and electricity, high density (heavy for their size), high melting point, ductile (most metals can be drawn out into thin wires) and malleable (most metals can be hammered into thin sheets). Different metals have different crystalline structures, e.g. cubic, hexagonal or monoclinic, which accounts for the different properties of each metal.

Metal alloys are composed of two or more elements, at least one of which is metallic. Alloys can be formed by one of two ways: substitution or interstitial.

Substitution occurs when an element of similar size is substituted into the lattice of another metal. Interstitial alloying occurs when a metal atom of a smaller size fits into the lattice of another metal without displacing another atom. Alloying is important because adding another element can increase strength and hardness.

In the medical industry, metals are used as load-bearing implants and internal fixation devices due to their high tensile, fatigue and yield strengths and their low reactivity. Specific applications of metals in the medical industry include: bone and joint replacement, dental implants, maxillary and craniofacial reconstruction and cardiovascular devices (Tresco 2006). Different metals are used for implants depending on the application but a few examples include: titanium and alloys, cobalt-chromium alloys, stainless steel and magnesium.

*2.1.2.2 Permanent Implants*

Permanent orthopedic implants may be associated with adverse local and remote tissue responses in some individuals. These adverse effects are mediated by the degradation products of implant materials (Jacobs, Hallab et al. 2003). Metal-on-metal bearings are used for total hip arthroplasties and have been associated with joint surface wear. Concerns over the increased use of metal-on-metal bearings have been voice due to the release of cobalt and chromium ions (Delaunay, Petit et al. 2010). Patients with metal-on-metal implants generally have higher serum and urine metal concentrations than those patients with conventional metal-on-polyethylene bearings. High metal concentrations in serum and urine may persist for the duration of the implant's lifetime (Jacobs, Hallab et al. 2003). Jacobs et al. studied a patient that had a total knee

arthroplasty. The patient had a serum titanium level of 536.8 PPB. The normal serum titanium level is approximately 4 PPB. The patient's high serum titanium level suggested a failed metal-backed patella. At the time of revision surgery on the patient, metal-on-metal contact between an area of polyethylene "wear-through" on the patellar component and the trochlear groove of the femoral component was identified. Figure 2.1 depicts the patient's failed patella at the time of the revision surgery. Figure 2.1a depicts the explanted patellar component. The inferior portion shows complete wear through; the central portion of the implant is cracked and delaminated. The vertical was created during component removal, using a high-speed rotary burr. Figure 2.1b shows the patient's titanium patellar baseplate. At the bottom of the component, there is burnishing, obvious wear, and abrasive loss of metal. This portion of the implant was articulating with the femoral component, after the patellar polyethylene had completely worn through. The vertical split was created during component removal using a high speed burr (Jacobs, Skipor et al. 2004).

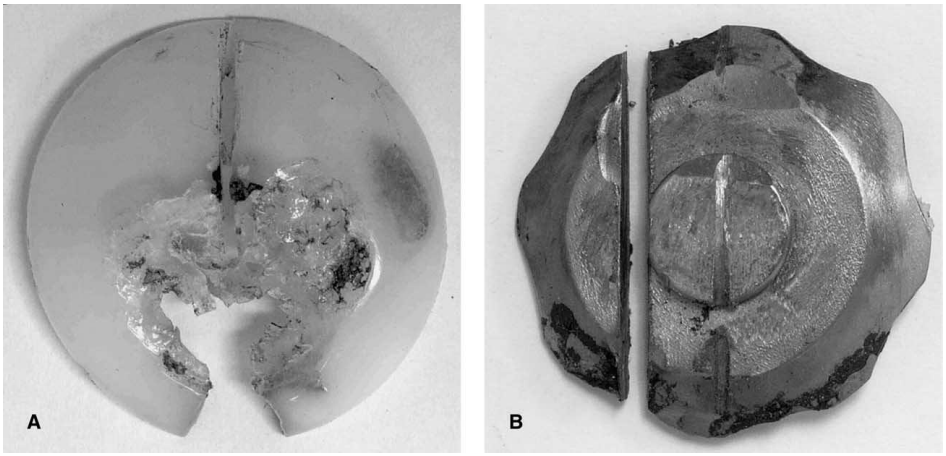


**Figure 2.1. (a) Explanted patellar component. (b) Titanium patellar baseplate (Jacobs, Skipor et al. 2004).**

Along with concerns over increased serum and urine metal concentrations, permanent implants, commonly made from titanium, stainless steel or a cobalt-chromium (Co-Cr) alloy, are known to lead to stress shielding. Stress shielding occurs because the metal implants are much stiffer than bone and this leads to a reduction of mechanical stimulus to the surrounding bone, causing bone resorption (Pettersen, Wik et al. 2011). Severe bone loss creates a problem for revision surgery, as it makes it difficult to safely remove the old prosthesis and provide proximal stability for the new prosthesis. Therefore, it is desirable that the implant maintains the physiological loading of the bone in order to limit the degree of bone resorption (Glassman, Bobyn et al. 2006).

*2.1.2.3 Magnesium as a Biodegradable Implant*

Within the past few years, the interest in magnesium and its alloys as innovative biodegradable materials has increased (Zberg, Uggowitzer et al. 2009). Magnesium is not only biocompatible, but also essential to human metabolism as a cofactor for many enzymes; therefore, the degradation products of a magnesium implant would not be toxic to the human physiology. According to Staiger et al., magnesium ions that are released as a result of the degradation aid the growth and healing of tissues (Staiger, Pietak et al. 2006). Further, any excess magnesium as a result of corrosion is harmlessly excreted through the urine (Saris, Mervaala et al. 2000). The physical and mechanical properties of magnesium make it quite suitable as a biodegradable metal implant, namely low density ($\rho$) = 1.74 – 2.0 g $cm^{-3}$, and elastic modulus (E) = 41-45 GPa. Both the density and elastic modulus of magnesium are similar to the corresponding properties of human bones as seen in Table 2.1 whereas the corresponding properties of a titanium alloy, stainless steel,

a Co-Cr alloy and synthetic hydroxyapatite differ greatly from the properties of human bone.

**Table 2.1. Summary of the physical and mechanical properties of various implant materials in comparison to natural bone (Staiger, Pietak et al. 2006).**

| Properties | Natural bone | Magnesium | Ti alloy | Co-Cr alloy | SS | Synthetic HA |
|---|---|---|---|---|---|---|
| **Density ($g/cm^3$)** | 1.8-2.1 | 1.74-2.0 | 4.4-4.5 | 8.3-9.2 | 7.9-8.1 | 3.1 |
| **Elastic modulus (GPa)** | 3-20 | 41-45 | 110-117 | 230 | 189-205 | 73-117 |
| **Compressive yield strength (MPa)** | 130-180 | 65-100 | 758-1117 | 450-1000 | 170-310 | 600 |
| **Fracture toughness ($MPam^{1/2}$)** | 3-6 | 15-40 | 55-115 | N/A | 50-200 | 0.7 |

Due to the tendency of magnesium and its alloys to corrode very quickly in chloride solutions, it is interesting that magnesium could still be used in biodegradable temporary implant devices such as plates, wires, stents, pins and screws, thus eliminating the need for a second surgery (Choudhary and Raman 2012). The properties of magnesium as well as its biocompatibility with the body make it a good material selection for use as a biodegradable implant.

### *2.1.3 Ceramics*

A ceramic is an inorganic, nonmetallic solid that may have a crystalline or partly crystalline structure; or may be amorphous, lacking any crystalline structure. Important

properties of ceramics include high strength, wear resistance, corrosion resistance, biocompatibility and thermal shock resistance. The term "structural ceramic" refers to ceramics used in a variety of applications such as the automotive and medical industries. Structural ceramics remain hard, resist deformation at high temperatures, resist cavitation and ablative wear and are inert, e.g. bio ceramics such as hip joint, knees, teeth and bone compatibility (Ceralink 2008). For most applications, high density and fine grain sizes in a ceramic are desirable because this gives higher hardness and better uniformity and strength as well as controlled porosity.

Another class of ceramics is that of bioceramics. Bioceramics range in biocompatibility from the ceramic oxides, which are inert in the body, to the other extreme of resorbable materials, which are eventually replaced by the materials which they were used to repair. Bioceramics are closely related to either the body's own materials or are extremely durable metal oxides. Hydroxyapatite (HA) is a bioceramic with a chemical structure very similar to the structure of bone. HA is used as a coating for metal surgical implants. Aluminum oxide, $Al_2O_3$, is used for prosthetic devices due to its excellent strength (Hickman 1999).

### *2.1.4 Polymers*

Polymers are composed of small units called monomers that are bound together by covalent bonds and form a chain. The chain formed can be linear or highly branched based on the monomers forming the chain. Synthetic polymers are the most commonly used biomaterial and can be classified into three categories: elastomers, thermoplastics and thermosets. Elastomers exhibit high elasticity, impact resistance and gas

permeability. Due to these properties, elastomers are widely used in cardiovascular and soft-tissue applications. Mostly commonly used elastomers are polyurethane block copolymers and silicone rubbers. Thermoplastics are polymers that can undergo reversible melt-solid transformation on heating. This property of thermoplastics makes them easy to process or to reprocess. An example of a thermoplastic is the polymer polyisobutylene. Thermoset polymers are the least used of the polymers due to their inability to undergo solid-melt transformation on heating. Epoxies and acrylics are examples of thermoset polymers. When used in the body, those synthetic polymers that are broken down into molecules that can be resorbed into the body or eliminated as waste are considered to be biodegradable. Biodegradable polymers are currently used in sutures and drug delivery systems. Polylactic acid (PLA) is a thermoplastic polymer currently used in stents, sutures and dialysis media. PLA has a degradation time of a few years (Nita 2011).

## 2.2 Corrosion of Magnesium

### *2.2.1 Introduction*

Corrosion is generally defined as the destruction of a metal due to a chemical reaction between the metal and the environment. According to Zeng et al., the reason for the poor corrosion resistance of magnesium and its alloys lies on two aspects: 1) the oxide films forming on the surface are not perfect and protective; 2) galvanic or bimetallic corrosion can be caused by impurities (Zeng, Zhang et al. 2006). Magnesium is highly reactive to oxygen; therefore, bulk magnesium forms a protective layer of

magnesium oxide when exposed to air. Imperfections in the oxide film, lead to magnesium and its alloys undergoing pitting corrosion as well as galvanic corrosion.

### *2.2.2 Methods of Corrosion*

#### *2.2.2.1 Pitting Corrosion*

Magnesium is a naturally passive metal. Pitting corrosion will occur at the free corrosion potential of magnesium, when it's exposed to chloride ions in a non-oxidizing medium (Song and Atrens 1999). Song et al. provided a model of the pitting corrosion mechanism of an as-extruded AM60 magnesium alloy depicted in Figure 2.2.

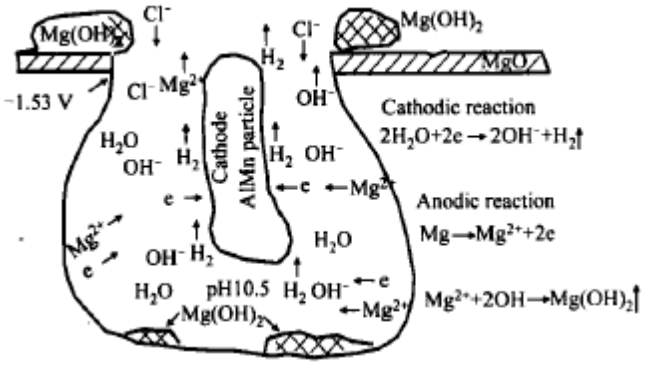


**Figure 2.2. Schematic of pitting corrosion mechanism for magnesium alloy AM60 (Song and Atrens 1999).**

The mechanism of pitting corrosion can be explained by the following steps:

1) Firstly, the alloy has a protective oxide film in air. The potential of MgO is +1 V.
2) When it is immersed in a sodium chloride aqueous solution, $Cl^-$ ions will absorb on the α areas bordering on AlMn particles.

3) If the breakdown potential of the oxide film reaches its free corrosion potential ($\varphi_{corr}$ = -1.53 V for AM60), then the α-matrix as an anode, compared to AlMn particles, starts to dissolve, and a corrosion nucleus may form near an AlMn particle.

4) The nucleus develops a corrosion pit, this may result in Mg $(OH)_2$ formation and hydrogen evolution according to the chemical reactions:

   Anodic reaction:

$$Mg \rightarrow Mg^{2+} + 2e \tag{2.1}$$

   Cathodic reaction:

$$2H_2O + 2e \rightarrow 2H_2\uparrow + 2OH^- \tag{2.2}$$

Total reaction:

$$Mg^{2+} + 2H_2O = Mg(OH)_2 + 2H_2\uparrow \tag{2.3}$$

5) At the end, an occlusion cell or a hemi-spherical corrosion pit will be formed with the corrosion proceeding. The pH value will finally reach and keep at 10.4 – 10.5. Magnesium hydroxide precipitates on the bottoms of pits and surfaces of samples (Song and Atrens 1999).

Pitting corrosion is a form of extremely localized corrosion that leads to the creation of small holes in the metal. Pitting corrosion occurs due to the depassivation of a small area, which becomes anodic while an unknown but potentially vast area becomes cathodic, leading to very localized galvanic corrosion (Wikipedia 2012).

*2.2.2.2 Galvanic Corrosion*

Galvanic corrosion is the corrosion that takes place when different metals or alloys are coupled together in the presence of an electrolyte. The position of the dissimilar metals in the galvanic series, the conductivity of the electrolyte and the ratio of the surface areas of the dissimilar metals are factors which affect the severity of the corrosion (AAC Ltd. 2010). Figure 2.3 depicts the galvanic series of metals listed according to their potential. Magnesium is the least noble, or most anodic of metals with a potential of -1.7V, meaning that magnesium is very susceptible to galvanic corrosion. Magnesium's alloys are susceptible to galvanic corrosion due to excessive levels of heavy metal and to poor design and assembly practices (Zeng, Zhang et al. 2006). In order for magnesium or any other metal to undergo galvanic corrosion, there are three conditions that must be met. The first condition states that the two metals have dissimilar potentials. The second condition requires the metals to be in contact while the third condition stipulates that the metal junction be bridged by an electrolyte (Corrosionist 2012). Almost any fluid can act as an electrolyte with the exception of distilled water. The electrolyte provides a means for ion migration whereby metallic ions can move from the anode to the cathode. Figure 2.4 illustrates the principle of galvanic corrosion around a bolt assembly. Also shown in Figure 2.4 are the anodic (dissolution of magnesium) and the cathodic (formation of hydrogen) reactions (Skar 1999).

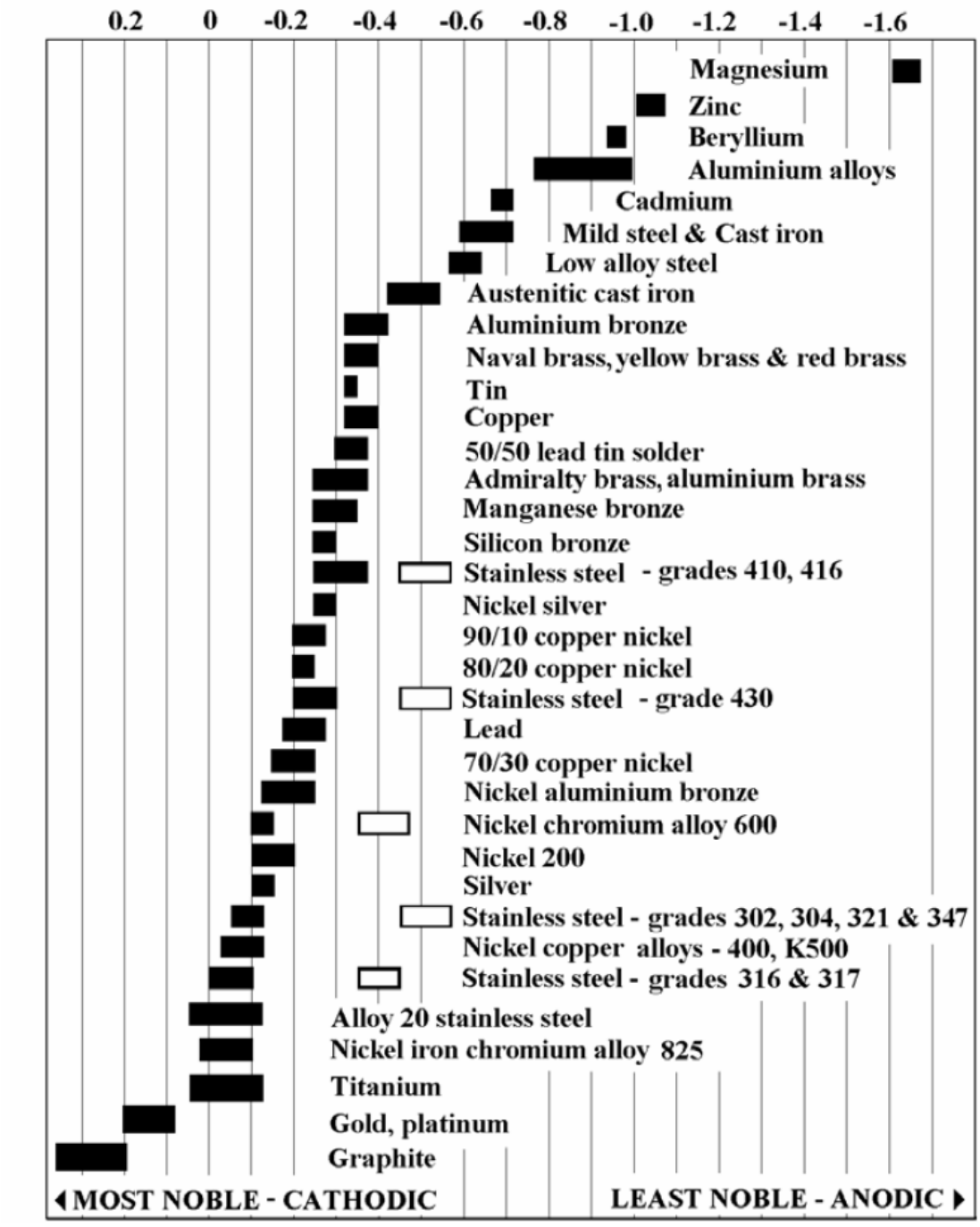


**Figure 2.3. A galvanic corrosion chart. Contains the electrochemical series ranks of metals according to their potential (Corrosionist 2012).**

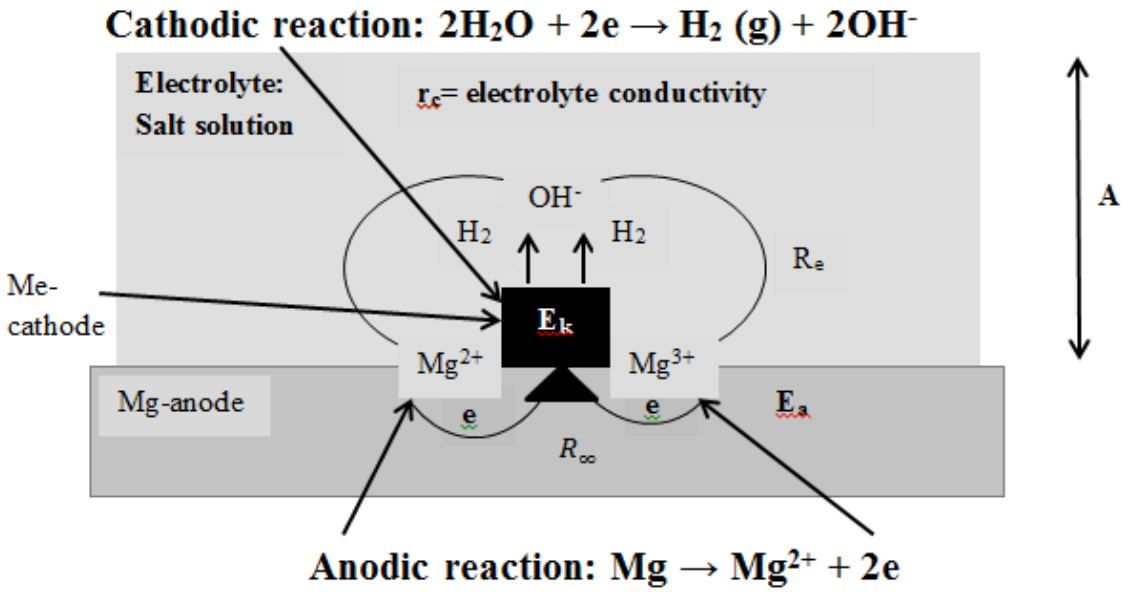


**Figure 2.4. Principle of galvanic corrosion. $E_k$ and $E_a$ = open circuit potential for cathode and anode, respectively. $F_a$ = metal resistance. $R_e$ = electrolyte resistance (Skar 1999).**

To limit galvanic corrosion, the current, I, in Equation (2.4) must be as low as possible, where $E_k$ and $E_a$ are the cathodic and anodic open circuit potentials, $R_a$ is the anodic polarization resistance, $R_k$ is the cathodic polarization resistance, $R_e$ is the electrolyte resistance and $R_m$ is the metal resistance. Equation (2.4) can be reduced as shown because $R_k$ and $R_e$ are much greater than $R_a$ and $R_m$.

$$I = \frac{E_k - E_a}{R_k + R_a + R_e + R_m} \approx \frac{E_k - E_a}{R_k + R_e} \qquad (2.4)$$

J.I Skar suggests that the reduction of the current can be achieved by proper material selection, proper design of the assembly and selective use of coatings and insulation materials (Skar 1999).

*2.2.2.3 Stress Corrosion Cracking*

Stress corrosion cracking (SCC) is characterized by the growth of cracks in a material that is exposed to a corrosive environment. According to the National Physical Laboratory, SCC is a deceptive form of corrosion. While SCC produces a marked loss of mechanical strength with little metal loss, the damage SCC causes is not noticeable to casual inspection and the cracks created can trigger mechanical fast fracture and catastrophic failure of components and structures. While SCC can lead to major disasters, the occurrence of SCC depends on the simultaneous achievement of three requirements: a susceptible material, an environment that causes SCC for that material and sufficient tensile stress to induce SCC (Cottis 2012). During the literature search, it was found that most literature in regards to SCC dealt with magnesium alloys. Die-cast alloys are more susceptible to SCC than those magnesium alloys that are rapidly solidified or semi-solid cast (Winzer, Atrens et al. 2005). Magnesium alloys can exhibit stress corrosion cracking in a variety of solutions such as high purity water, sodium bromide (NaBr), sodium chloride (NaCl), sodium hydroxide (NaOH) and hydrogen chloride (HCl) solutions (Miller 1993).

There are two forms of SCC: transgranular SCC (TGSCC) and intergranular SCC (IGSCC). TGSCC is the most common form of SCC in which the cracks follow the edges of the crystal lattice and intergranular stress corrosion cracks follow the grain boundaries of the metal (Zeng, Zhang et al. 2006). Figure 2.5 and Figure 2.6 depict the two forms of SCC: TGSCC and IGSCC, respectively.

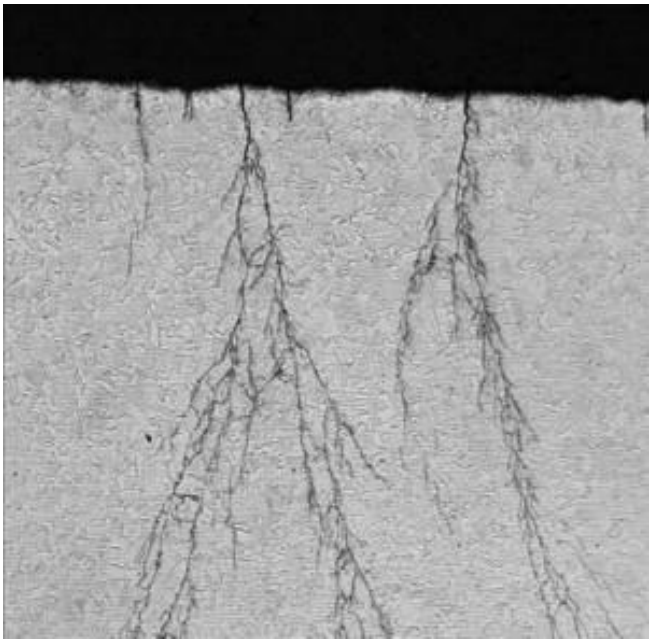

**Figure 2.5. Transgranular stress corrosion cracking in a metal (Ahluwalia 2012).**

**Figure 2.6. Intergranular stress corrosion crack. The crack follows the grain boundaries (Metallurgical Technologies 2012).**

### *2.2.3 Methods to Prevent Corrosion*

#### *2.2.3.1 Coatings*

Surface modification by coatings has become an essential step to improve the surface properties of magnesium, such as wear, corrosion and oxidation (Altun and Sen 2006). Due to the susceptibility of magnesium and its alloys to corrosion and wear, coating the surface provides a way to prevent or lower the rate of corrosion. Altun *et al.* determined that physical vapor deposition (PVD) multilayered coatings of aluminum nitride (AlN), (AlN + AlN + AlN), and aluminum nitride plus titanium nitride (TiN), (AlN + TiN) deposited on AZ91 magnesium alloy increased the corrosion resistance of the alloy. Although the corrosion resistance of the alloy was increased, it was observed that small structural defects such as pores and cracks were forming in the coatings after corrosion tests. Figure 2.7 depicts a micro-crack that formed in a AlN + TiN coating after the completion of a corrosion test (Altun and Sen 2006).

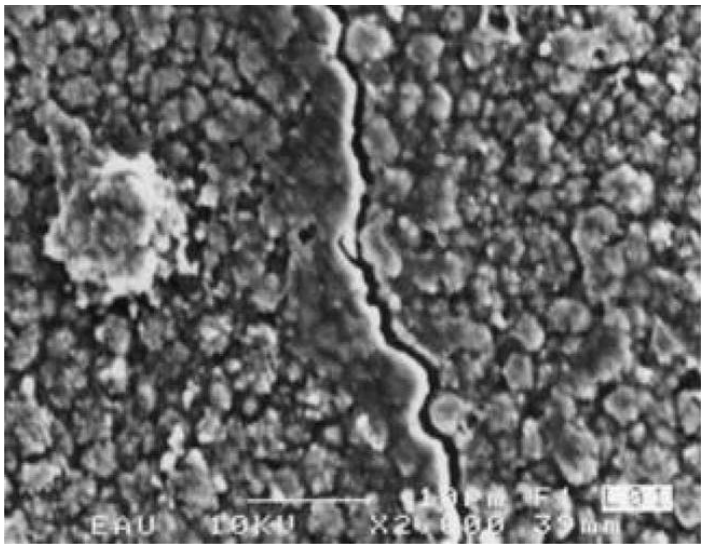

**Figure 2.7. A micro-crack formed in the AlN + TiN coatings after corrosion experiments (Altun and Sen 2006).**

Wu et al. deposited a ceramic/metal coating, $Al_2O_3$/Al onto the surface of AZ31 magnesium alloy samples by a magnetron sputtering system. After deposition, atomic force microscopy (AFM) was used to determine that all coatings took on a compact, <1 μm, surface morphology in micro-regions. Coated and uncoated AZ31 samples were placed in 3.5 wt% NaCl solution. The uncoated material showed active dissolution, while the coated samples showed passivation. The coated sample's passivation is mainly due to the presence of the $Al_2O_3$ coating. The passivation of the coated sample also indicated that the coating was inhibiting the anodic process; by acting as a barrier to the electrolyte, the coating impeded the electrolyte's contact with the substrate surface (Wu, Zeng et al. 2006). Coatings can protect a substrate by providing a barrier between the metal and its environment and/or through the presence of corrosion inhibiting chemicals in them (Gray and Luan 2002).

Currently, thin films of zinc oxide are being utilized for the production of transparent and electrically conductive devices. An investigation into the degradation of zinc oxide thin films indicated that the electrode behavior of a polycrystalline zinc oxide is strictly related to the pH of the solution. In low pH range, the zinc oxide dissolves to give divalent ions by Reaction (2.5):

$$ZnO + 2h^{+} \rightarrow Zn^{2+} + 1/2O_2 \text{ (De, Perugini et al. 2001).} \qquad (2.5)$$

## 2.3 Magnetron Sputtering

### *2.3.1 Introduction*

Sputtering is the removal of atomized material from a solid by energetic bombardment of its surface layers by ions or neutral particles (Morley). Any thin film

deposition process involves three main steps: (1) production of the appropriate atomic, molecular or ionic species, (2) transport of these species to the substrate through a medium and (3) condensation on the substrate, either directly or via a chemical and/or electrochemical reaction, to form a solid deposit (Wasa 1992). Magnetron sputtering uses strong electric and magnetic fields to trap electrons close to the surface of the magnetron, also known as the target (Wikipedia 2012). The materials utilized as deposition substrates can range from silicon wafers to glass. Reasons for sputtering include using large-area-targets which gives uniform thickness over the substrate, ability to control the thickness by deposition time and other parameters and to sputter clean the surface in vacuum prior to deposition (Ginsburg 2002).

### *2.3.2 Radio Frequency Sputtering*

With radio frequency (RF) sputtering, when an RF potential, with a large peak-to-peak voltage, is capacitively coupled to an electrode, an alternating positive/negative potential appears on the surface. Due to this alternating potential, it is possible to use RF sputtering to sputter electrically insulating materials (Mattox 2010). RF sputtering also offers advantages in that film depositions can be carried out at low temperatures while yielding preferred orientation and uniform properties (Dang, Fu et al. 2007). One disadvantage of sputtering dielectric targets using RF sputtering is the generation of large thermal gradients that can fracture the target if high power levels are used. Large thermal gradients develop due to electrically insulating materials, usually brittle materials, having poor thermal conductivity (Mattox 2010).

### *2.3.3 Direct Current Sputtering*

Direct current (DC) sputtering is a form of material deposition that involves bombarding a target with ionized gas molecules. When the target is bombarded with gas molecules, a displacement of target atoms occurs. These free target atoms adhere to a negatively charged substrate creating a thin film on its surface. DC sputtering technique can be non-reactive or reactive. If a ceramic target is being utilized, to ensure that the resulting film will also be a ceramic, oxygen can be flowed into the system to ensure that the metal ions will react with oxygen to form a ceramic.

### *2.3.4 Reactive Sputtering*

Reactive sputtering occurs when a gas is purposely added to the sputtering chamber to react with the sputtered material (Sproul, Christie et al. 2005). The reactive sputtering process can be divided into three modes: (1) metallic, (2) transition and (3) reactive. A typical characteristic of the reactive magnetron sputtering is a low deposition rate of compounds produced in the reactive mode compared to that of the pure metallic films produced in the metallic mode. The decrease in deposition rate of films sputtered in the reactive mode is due to a reaction of the reactive gas with the surface of the sputtered target and its conversion to a compound (Musil, Baroch et al. 2005). Reactive sputtering can occur in three different locations within the sputtering chamber: (1) on the substrate,

(2) within the plasma or (3) on the metal target as shown in Figure 2.8.

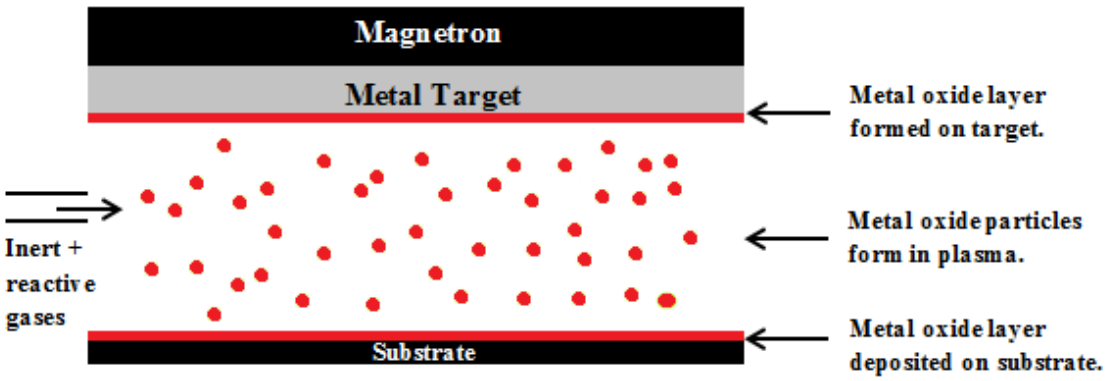


**Figure 2.8. Locations of reactive sputtering.**

If the reaction between metal ions and reactive gas occurs on the metal target, a thin dielectric layer will form on the metal target; often referred to as target poisoning. With the buildup of an insulating layer on the surface, positive ions accelerated in the plasma collect on the target surface and charge the insulating layer. The voltage buildup is referred to as arcing and can cause serious problems to the target. When arcing occurs, the target material can melt at localized points. This material is ejected and can damage the material being processed and it accumulates on other surfaces. This erosion can contaminate the source as well as degrade the target (Grove 2000). There are two ways to suppress or eliminate arcing: (1) to eliminate un-eroded areas and (2) to remove the accumulated charge from insulated surfaces on the un-eroded areas (Musil, Baroch et al. 2005). It is the second solution that was utilized in this study. The accumulated charge was removed from the insulated surface by using pulsed dc sputtering.

### *2.3.5 Pulsed DC Reactive sputtering*

PDC sputtering can be used to prevent arcing. PDC power interrupts the voltage buildup by applying a short positive pulse to the target (Kelly, Henderson et al. 2000). Figure 2.9 shows a typical voltage sequence used in PDC sputtering. The power is applied to the target for a time $\tau_{on}$, the 'on-time' during which a negative voltage pulse of a few hundred volts is applied to the target. At the end of an 'on-time', the power is switched to a small positive voltage. Electrons are attracted to the target through this positive pulse and this flux negative particles will partially or fully discharge the insulating layer (Belkind, Freilich et al. 2005).

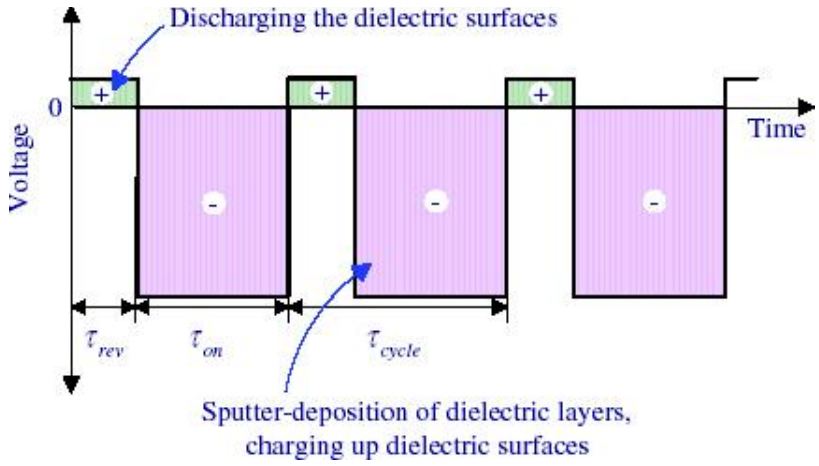


**Figure 2.9. Ideal voltage sequence applied to asymmetric bi-polar PDC sputtering of dielectrics (Belkind, Freilich et al. 2005).**

Fully discharging the insulting layer on the target will result in a pure metal target again. Kelly et al. found that periodic target voltage reversals effectively discharge poisoned regions on the target (Kelly, Henderson et al. 2000). This finding is important because target poisoning leads to arcing. If the occurrence of poisoning is decreased or

diminished, then the occurrence of arc events at the target will also decrease. The decrease in occurrence of arcing will stabilize the deposition process. Using PDC sputtering, high-quality defect-free metal oxide films can be deposited without fear of target poisoning and arcing.

# CHAPTER 3

# MATERIALS, EXPERIMENTS AND METHODS

## 3.1 Fabrication

### *3.1.1 Magnetron Sputtering*

Throughout the study, the AJA International, Inc. ATC 1800 F magnetron sputtering system was utilized to develop the metal oxide films and can be seen in Figure 3.1.

**Figure 3.1. AJA International ATC 1800 F Magnetron Sputtering system at NCAT.**

The AJA International magnetron sputtering system is composed of three targets and can be used to perform radio frequency (RF) sputtering, direct current (DC) sputtering or pulsed-direct current (PDC) sputtering. RF sputtering can be utilized at a

maximum power level of 500 W while the DC sputtering power level is much higher at 1000 W; still higher is the maximum power level of PDC sputtering which is 5000 W. Although RF sputtering is known to produce high quality thin film coatings that are good for insulating materials, it is a slow process with low deposition rates. DC reactive sputtering also has low deposition rates and is known for being problematic when depositing oxides. Also, when using DC reactive sputtering, arcing can occur at the target, poisoning the system. To avoid low deposition rates and possible arcing, PDC reactive sputtering was used to produce high quality films with high deposition rates.

The substrates were loaded into the AJA International magnetron sputtering system via the loading dock. Once placed into the loading dock, the substrates were loaded into the main chamber. The magnetron sputtering system is operated under a high vacuum, which is maintained by a turbomolecular pump. Located in the main deposition chamber, a rotating stand allows the substrates to rotate at a constant speed to ensure an evenly distributed coating. Along with substrate rotation, the system has a residual gas analyzer (RGA). The RGA monitors the distribution of the gas within the chamber and it is this constant monitoring that allows for deposition parameters to be precisely copied at a later time resulting in the development of reproducible coatings.

When using PDC sputtering technique, it is important to know the deposition rate of a certain material under optimal parameters. Knowing the deposition rate of a material allows the time of deposition to be determined so that a certain thickness of film can be developed. Along with knowing the deposition rate, it is also important to know how much oxygen will need to be introduced into the system for the metal ions to react with.

An oxygen flow calibration was completed by increasing the oxygen flow into the system and then measuring the transparency of the coating. Each sample was deposited for the same amount of time so that height measurements could be completed and the resulting deposition rates comparable.

Aluminum was the first metal target used and the deposition parameters used can be seen in Table 3.1. Each sample was deposited with a power of 150 W for 409 s at room temperature in an atmosphere with 20sccm of argon under a working pressure of 2 mTorr. To begin the oxygen flow calibration, the parameters used for the power, argon flow and time settings were suggested. The oxygen flow for the calibration ranged from 0 sccm to 4 sccm in 1 sccm increments.

**Table 3.1. Deposition parameters for oxygen flow calibration.**

| Material | Working Pressure (mTorr) | Argon (sccm) | $O_2$ (sccm) | Time (s) |
|---|---|---|---|---|
| Al | 2 | 20 | 0 - 4 | 409 |
| Fe | 2 | 20 | 0 - 17 | 600 |
| Zn | 2 | 30 | 0 - 20 | 900 |

Another aspect to consider when using PDC sputtering technique is calibration of different targets. Iron was the next target used in the sputtering system and it was crucial that an oxygen flow calibration was completed to determine which oxygen flow produced a ceramic as well as had a good deposition rate. Table 3.1 lists the deposition parameters used for the oxygen flow calibration for the iron target. Each sample was deposited with a power of 150 W for 600 s in an atmosphere with 20 sccm of argon. The oxygen flow utilized for the calibration ranged from 0 sccm to 17 sccm.

Zinc was the last target used and required more samples to be deposited. Table 3.1 lists the deposition parameters for the oxygen flow calibration for the zinc target. The oxygen flow was initially increased by 1 sccm until the flow rate of 5 sccm was reached. When the samples showed no apparent change in transparency, the oxygen flow was increased by 5 sccm until the max flow of 20 sccm was reached. Upon visual inspection, the transparency of the sample changed when deposited with 10sccm compared to that at 5 sccm. Flows of 6, 7, 8 and 9 sccm were used to obtain the point at which a zinc oxide layer was being deposited.

## 3.2 Characterization

### *3.2.1 Profilometry*

To determine the thickness of the ceramic coatings, an Alpha-Step IQ Surface Profiler was utilized. The profiler uses a stylus scanning motion that provides exceptional measurement stability for extremely repeatable measurements (K.-T. Corporation 2010). In order to use the profiler's capabilities of step height analysis, it was important to have a sample that had a step. To make a sample, tape was placed on half of the substrate before deposition. After deposition, the tape was removed, thus creating a step in height between the substrate and coating. Figure 3.2 shows the Alpha-Step IQ Surface Profiler utilized during this study. The black region is the stage upon which the samples are placed. The small white box in the middle contains the stylus scanner. A feature of the profiler is the user's ability to create a recipe of parameters that can be used to ensure that repeatability of measurements is obtained. Table 3.2 shows the scanning parameters used in this study to obtain height measurements.

**Figure 3.2. Alpha-Step IQ Surface Profiler.**

**Table 3.2. Scanning parameters used as a recipe to obtain height measurements.**

| Leveling | Scan Length | Scan Speed | Sampling rate | Sensor range |
|---|---|---|---|---|
| 2 zones | 500 μm | 20 μm/s | 50 Hz | 20 μm |

Using those parameters given in Table 3.2, the sample was placed upon the stage and the stage height adjusted so the stylus could scan the surface. Figure 3.3 depicts the resulting graph after a scan. The x-axis is the scan length in micrometers, whereas the y-axis is the height in nanometers. As shown, there are two zones, left and right. The average height of each zone is taken and the difference between the right and left zones is given as the height of the coating. In this image, the thickness of the coating is approximately 75 nm. The sharp peak in Figure 3.3 can be attributed to the surface roughness of the substrate and/or residue from the tape used to create the step. The profiler was utilized throughout the entire study to obtain the height of each new sample created. It was imperative the

height of the sample was obtained by a reliable and reproducible method because the height was used to determine the deposition rate (nm/s).

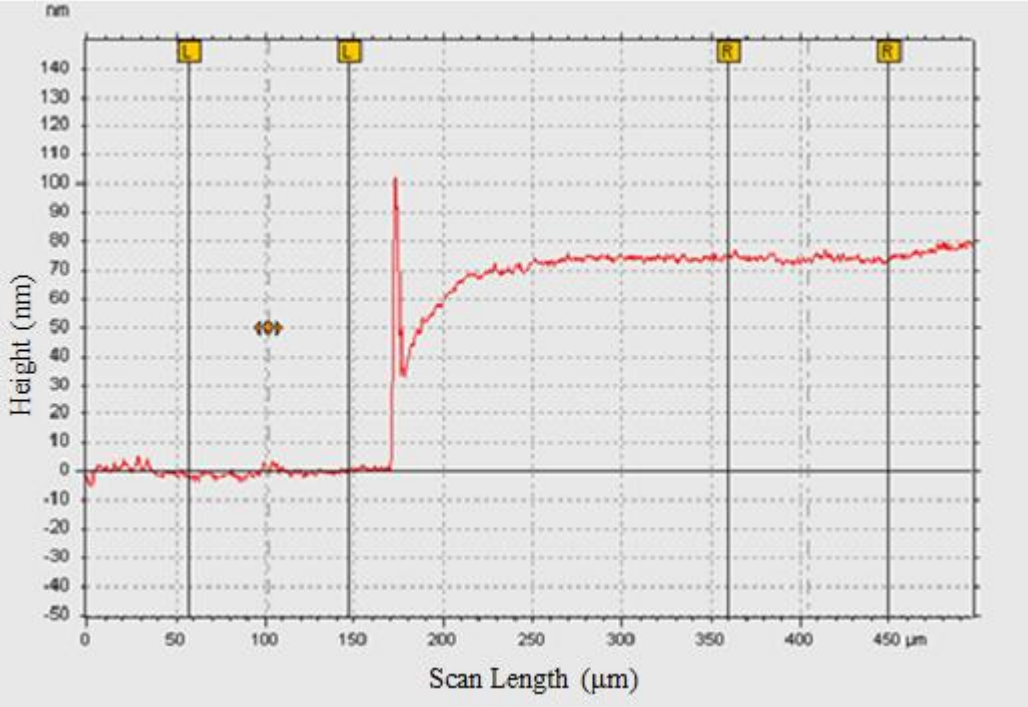


**Figure 3.3. Step height analysis utilizing leveling with 2 zones.**

### *3.2.2 Optical Microscopy*

To determine the transmittance of light through each sample, an optical density method was utilized. To complete this method, a Zeiss Axio Imager Upright Microscope, shown in Figure 3.4, was used to capture images of the coating, bare substrate and a dark background. Figure 3.5 shows the images captured by the optical microscope. These images of the coating, substrate and dark region were used to obtain the transmittance for one sample.

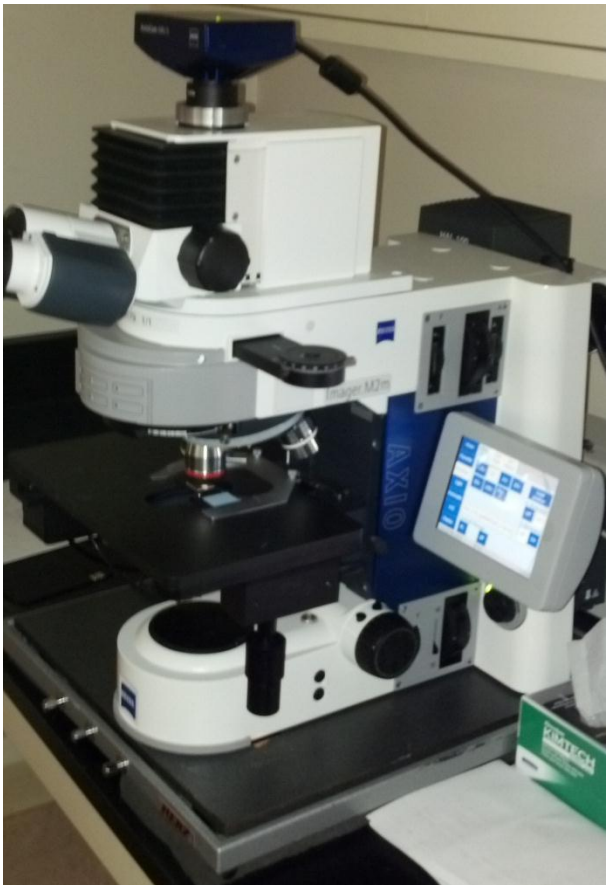

**Figure 3.4. Zeiss Axio Imager Upright Microscope at NCAT.**

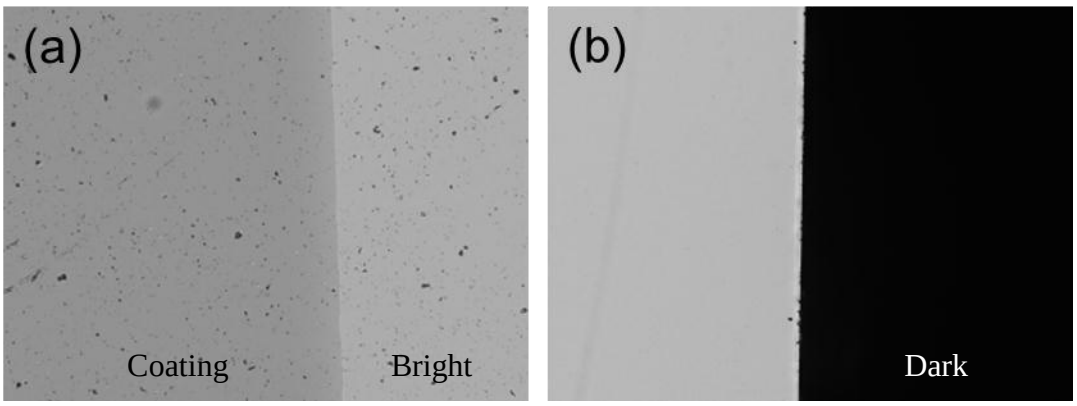


**Figure 3.5. Images obtained to measure transmittance of coatings. (a) Coating and bright regions. (b) Dark region.**

From these images, the optical density was extracted from each section via Image Pro Plus and plugged into Equation (3.1) to obtain the transmittance of the sample.

$$Transmittance\ (T) = \frac{Coating-Dark}{Bright-Dark} * 100 \quad (3.1)$$

where *coating* refers to the optical density of the coating, *dark* refers to the optical density of the dark region and *bright* refers to the optical density of the bare substrate.

To further the use of the optical density method, immersion tests were completed using multilayered magnesium and $Al_2O_3$ coatings of 10 nm, 15 nm and 20 nm thicknesses immersed in DeIonized (DI) water, phosphate buffered saline (PBS), Dulbecco's Modified Eagle Medium (DMEM) and various concentrations of saline. During the immersion tests, images were taken every 15 s over a time period until the magnesium layer, used as a detection device, was gone. Using Image Pro, the optical density of these images was obtained and used to compute the corrosion kinetics of the $Al_2O_3$ coating.

### *3.2.3 X-Ray Diffraction*

X-ray diffraction was performed throughout the duration of this study using the Bruker AXS D8 Discover, which can be seen in Figure 3.6. XRD is a high-tech, non-destructive technique for analyzing a wide range of materials with thin-films being just one example (Bruker 2012). XRD was used to determine the phase of a thin film. A phase is composed of a collection of molecules that can be arranged to form an amorphous or crystalline solid (Fewster 1996). Various thin films manufactured in this study were characterized by XRD to determine if the pattern of the thin film corresponded to the pattern of a material in the XRD database. Once the composition of

the film was determined, depositions were completed to produce more samples used in biological assays.


**Figure 3.6. Bruker AXS D8 Discover XRD machine at NCAT.**

### *3.2.4 Scanning Electron Microscropy*

The Hitachi SU8000 field emission scanning electron microscope, seen in Figure 3.7, utilizes a raster scan pattern. This type of pattern sweeps horizontally left to right then blanks and rapidly moves back to the left.

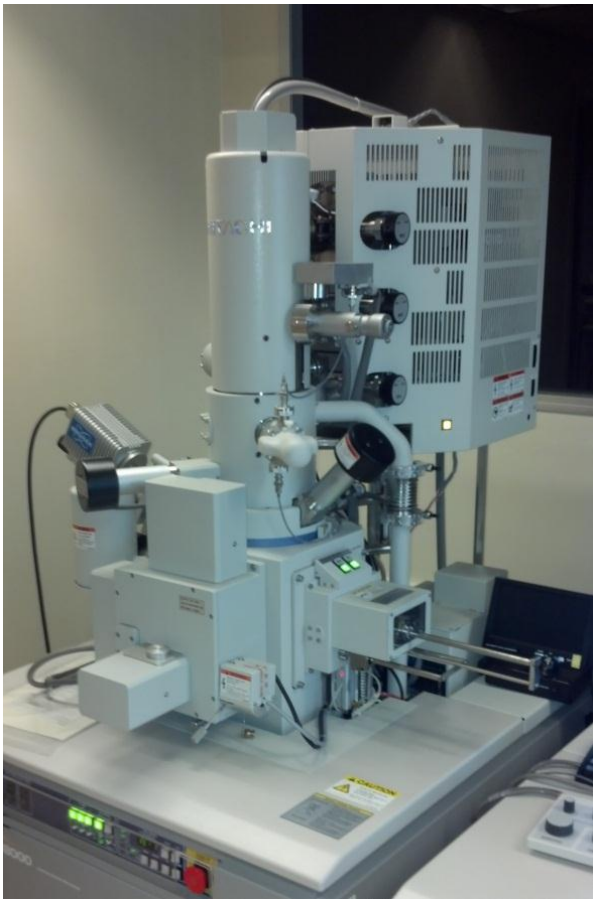

**Figure 3.7. Hitachi SU8000 Field emission scanning electron microscope.**

With this particular microscope, there was a variety of signal detecting systems available to the user depending upon what information was needed. A description of the information obtained when a certain signal type is used can be seen in Table 3.3, while Figure 3.8 models the location of each detector within the system. The SEM was utilized in this study to determine the crystal structure of the ceramics along with some topographical information; therefore the BSE and SE signal types were used, where BSE refers to back scattered electrons and SE refers to secondary electrons, respectively. Each coating was deposited on a silicon substrate.

**Table 3.3. Various signal detecting systems used on the FESEM to obtain optimized contrast for different purposes (Hitachi 2012).**

| Signal Type | Signal Name | Detector | Information |
|---|---|---|---|
| BSE | HA-BSE | Top | Composition, crystal |
| BSE | LA-BSE | Upper | Composition + Topographical (charge suppression) |
| SE | SE | Upper | Surface information (Including voltage contrast) |
| SE | Lower | Lower | Topographical |
| STEM | BF-STEM | STEM | Sample internal information + Crystal |
| STEM | DF-STEM | Lower | Sample internal information + Composition |

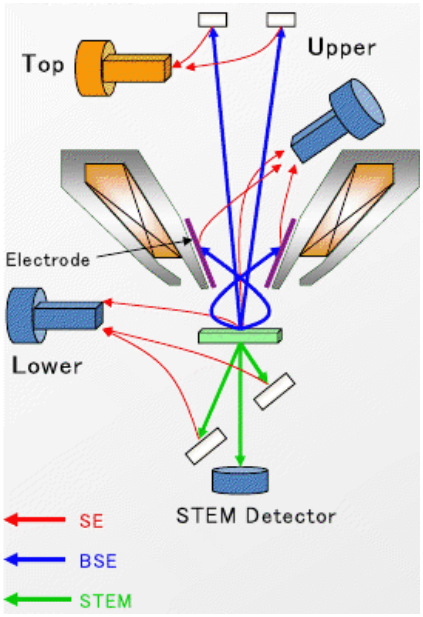


**Figure 3.8. Diagram of detectors used in Hitachi SU8000 FESEM (Hitachi 2012).**

Charging of the sample is the greatest impediment to obtaining good images in the SEM. Charging occurs when there is a buildup of excess electrons on the surface of the sample. The buildup of electrons creates an electric field which deflects the electron beam in undesirable ways. There are five common types of charging: general charging, edge charging, area charging, line by line charging and residual charging. General charging occurs when electrons buildup over the scan area resulting in an image that becomes increasingly bright to where the contrast and brightness adjustments cannot compensate. Edge charging is a type of charging where electrons buildup on high or isolated portions of the sample, which leads to uncharacteristically bright edges and small features in the image. With area charging, electrons charge and discharge in certain areas. Areas on the sample can become bright or dark without any adjustments of the SEM and can change continuously. Line by line charging occurs when electrons release from the sample causing bright streaks across the image. During residual charging, electrons are left from a previous scan and add to the electrons emitted by the current scan. Charging is common in non-conductive samples. To balance the incoming beam electrons to the outgoing sample electrons, i.e. reduce charging, the voltage can be reduced. Reducing the beam current and vacuum in the chamber will also reduce charging. Coating a non-conductive sample with a conductive layer such as gold (Au) makes the sample surface conductive thus eliminating charging (Rice 2012).

### *3.2.5 Atomic Force Microscopy*

Surface roughness was measured using a NT-MDT NTEGRA platform atomic force microscope, shown in Figure 3.9. Images were taken using semi-contact mode

using a super sharp tip with a curvature radius of 3-6 nm. Semi-contact mode is a mode in which the cantilever tip only makes contact with the sample surface occasionally. Semi-contact mode is often the preferred method of contact when completing surface roughness measurements because the force of pressure of the cantilever on the sample surface is low. The lower contact pressure allows measurements to be completed on softer and easy-to-damage materials such as polymers as well as reduces the risk of the cantilever tip breaking. Along with measuring surface roughness, semi-contact mode is used to determine other surface characteristics, such as elasticity and viscosity of the surface (NT-MDT 2012). Images were processed using Nova software supplied by NT-MDT.

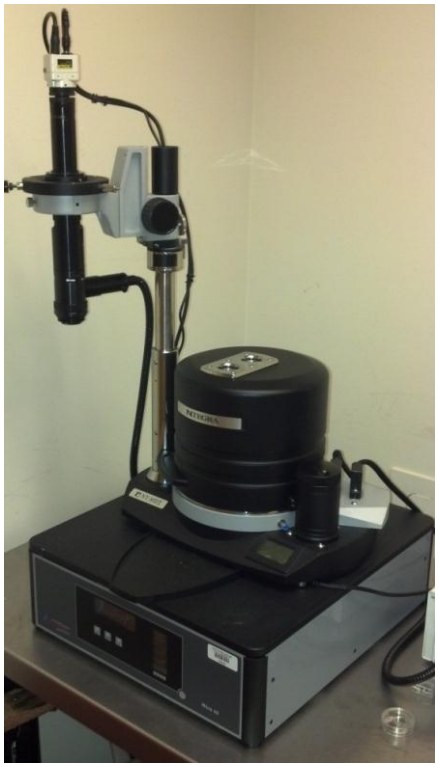

**Figure 3.9. NT-MDT NTEGRA platform atomic force microscope at NCAT.**

### 3.3 Biological Adhesion Assay

An adhesion assay was performed on all three ceramic coatings in order to determine their biological compatibility with human osteoblast cells from the cell line designation: hFOB 1.19, passage 3, from American Type Culture Collection, Mannassas, VA. To seed the osteoblasts, one vial of cells were removed from liquid nitrogen and warmed in a 37°C water bath for two minutes. Once the cells were thawed, they were combined with 45 ml of complete growth media. The formula to make roughly 500 ml of complete growth media can be seen in Table 3.4.

**Table 3.4. Formula for osteoblast complete growth media.**

| Description | Amount (ml) | Final Concentration |
|---|---|---|
| DMEM | 250 | 1:1 |
| Ham's F-12 | 250 | |
| FBS | 50 | 10% |
| Gentamicin Sulfate | 3.3 | 0.70% |

The 45 ml of cells with media were split into three T-75 flasks equally, where the cells were cultured until flasks were 80-90% confluent, approximately one week. The cells were grown at 37°C ensuring slowed cell division which results in a more mature osteoblast phenotype compared to those osteoblasts grown at 34°C. During the week of growth, the cell media was changed every two to three days. After the week of incubation, the cells were trypsinized from the culture vessels. Trypsinization is the method that utilizes trypsin, an enzyme which breaks down proteins, to dissociate the cells from the culture vessel. This method is often used to passage cells from a flask to a

culture vessel appropriate for the adhesion assay. For this assay, a 24 well plate was used. Figure 3.10 depicts the setup of the 24-well plate used for testing the alumina coating.

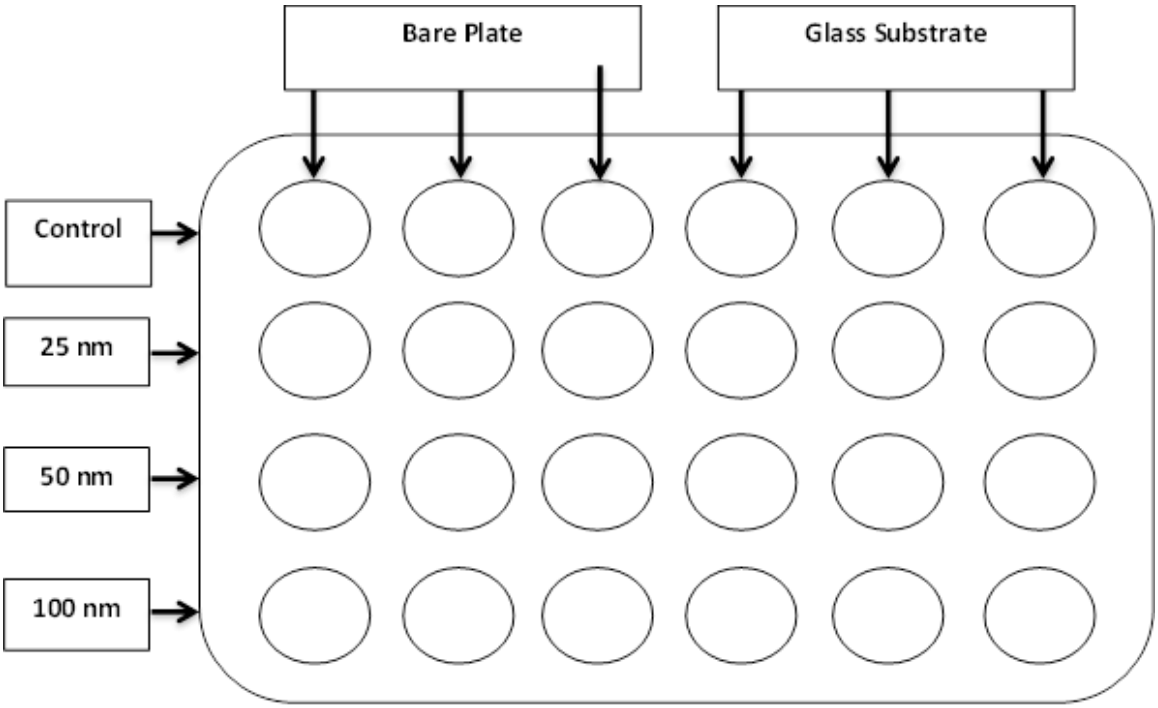


**Figure 3.10. Setup used for aluminum oxide coating adhesion assay.**

The top row of the 24-well plate was used as the control. The first three wells in the first row were empty, containing only cells. This control showed the ordinary growth of the osteoblast without any effect from a coating or glass substrate. The last three wells in the first row, contained bare class substrates. Again, having only the bare glass shows how the cells adhere to the substrate without any side effect from the alumina. The last three rows of the plate contained alumina coatings with thicknesses of 25, 50 and 100 nm respectively. The same 24-well plate setup was used for the iron oxide and zinc oxide coatings. However, the thicknesses of the iron oxide coatings were 50, 100, and 150 nm and the thicknesses of the zinc oxide coatings were also 50, 100 and 150 nm. Different

thicknesses were used for the iron oxide and zinc oxide coatings compared to the thicknesses of the alumina coatings because thinner coatings of the iron oxide and zinc oxide would not last for the four hours needed to perform the adhesion assay. After trypsinizing the cells from all three flasks, the cells were spun for 5 minutes at 1200 rpm. After spinning, the cells were in the form of a small pellet. This pellet was dispersed into 35 ml of media. Before beginning the adhesion assay, it was important to know the number of cells per milliliter so the total number of cells seeded into each well would be known. A 50:50 mixture of cells and 0.1% Trypan Blue solution were added to a hemocytometer. Figure 3.11 models the standard hemocytometer chamber.

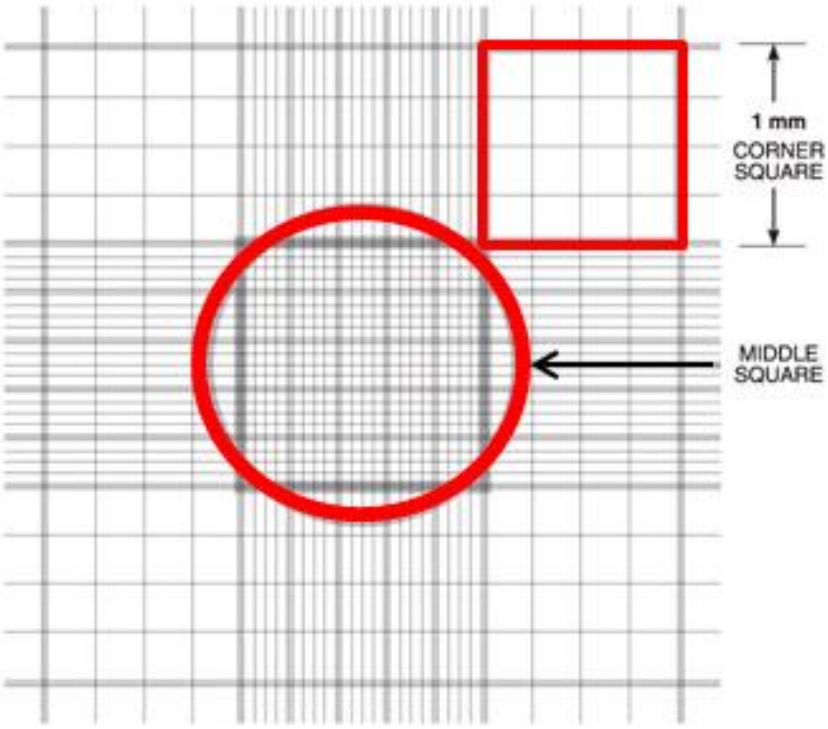


**Figure 3.11. Standard hemocytometer chamber (Frei 2011).**

To determine the number of cells per milliliter, all cells in the four 1 $mm^2$ corner squares, top right is shown in red, are counted. The cells stained blue were dead, while the living cells were transparent. Next, the average count of live cells is obtained by taking the average of the four values from each square, respectively. Equation (3.2) is used to determine the number of cells per milliliter.

$$\frac{Cells}{ml} = the\ average\ count\ per\ square * dilution\ factor * 10^4 \qquad (3.2)$$

The dilution factor is 2 due to the 50:50 mixture of cells to Trypan Blue solution. The total number of cells is found by multiplying the cells per milliliter by the original volume of fluid from which the cell sample was removed.

A total of 25 million viable cells were grown between the three T-75 flasks for the adhesion assay. A final concentration of $3.33*10^5$ live cells per ml was seeded into each well. More cells than usual were seeded into each well to counter the limited time the cells had to adhere. The plates were then placed in the incubator at 37°C for four hours to allow the cells to adhere to the coatings. After four hours, the media as well as any cells that did not adhere to the coatings were aspirated and the coatings were washed with 1X PBS pH 7.4. Using an optical microscope, the cells that adhered to the coatings were seen and the percent confluency of the adhered cells was estimated. Percent confluency was estimated by determining what percentage of the coating the cells had attached, e.g. 50%.

**3.4 LIVE/DEAD Cell Viability Assay**

Using the LIVE/DEAD Viability/Cytotoxicity Assay Kit from Molecular Probes (M.P. Inc. 2005), a two-color fluorescence cell viability assay was performed to determine the number of live and dead cells after the cells were cultured with the

"soaked" media described below. The soaking test was performed before the LIVE/DEAD assay. All coatings used were 100 nm to ensure the coating would not degrade before the soaking period was over. Aluminum oxide, ferric oxide and zinc oxide coatings were soaked for 1 day and 3 days with 200 µl of complete growth media, which will be referred to as "soaked" media. After soaking for 1 day, the used media was then diluted with fresh media. A concentration gradient was used to establish a dose-response relationship. Figure 3.12 depicts the layout of the 96-well plate. Each color corresponds to a certain percent concentration of soaked media to new media.

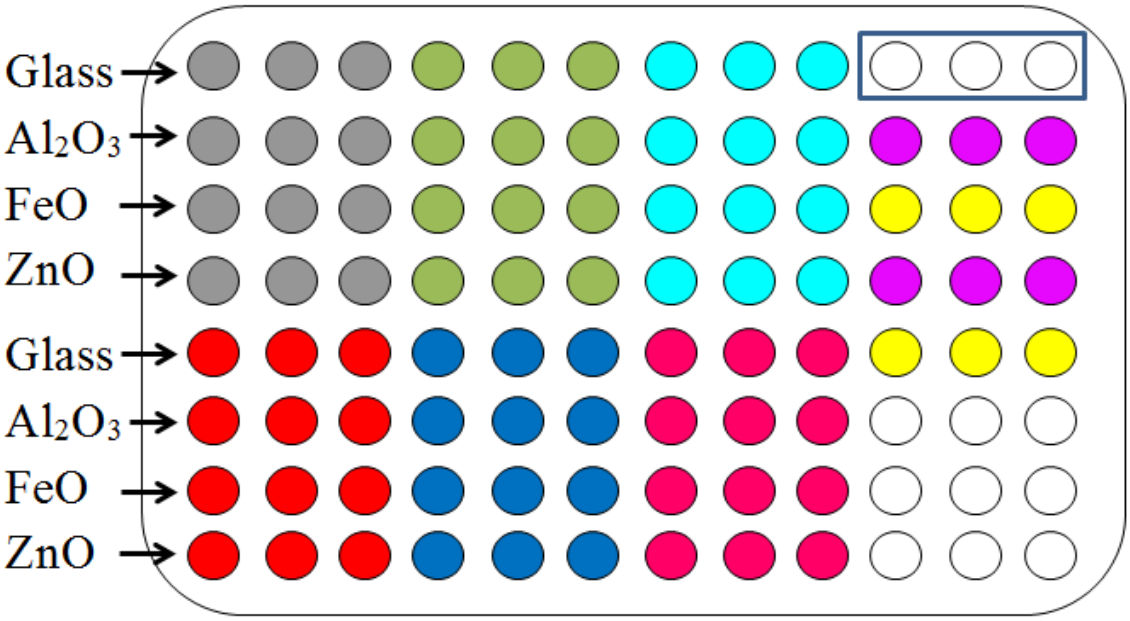


**Figure 3.12. LIVE/DEAD assay setup.**

The gray region represents those wells with 0% solution, with 0 µl of used media to 200 µl of new media. The green region is a 1% solution, with 2 µl of used media to 198 µl of new media. The teal region is a 5% solution, with 10 µl used media to 190 µl of

new media. The red region represents a 12.5% solution, with 25 μl of used media to 175 μl of fresh media. The blue region represents a 25% solution, with 50 μl of used media to 150 μl of new media. The pink region represents a 50% solution, with 100 μl of used media to 100 μl of new media. The top purple four wells represent live cells with ethidium homodimer-1 (EthD-1) while the bottom purple four wells represent dead cells with EthD-1, respectively. The top yellow four wells represent live cells with calcein while the bottom yellow four wells represent dead cells with calcein, respectively. Those wells boxed in contain no cells, while the remaining twelve wells were left blank.

This same setup was repeated using media that soaked the coatings for three days. Along with measuring the effects of the concentration of used to new media, soaking the coatings for both 1 day and 3 days will determine if the toxicity level will increase due to the media's increased exposure to the coatings.

# CHAPTER 4

# RESULTS AND DISCUSSION

## 4.1 Fabrication

### *4.1.1 Magnetron Sputtering*

After completing the oxygen flow calibration for the aluminum target, the height measurements were taken so the deposition rate could be determined. Table 4.1 shows the thickness of each sample, the deposition rate and the resulting rate of deposition. As seen, the deposition rate decreased as the oxygen to argon ratio increased. When too much oxygen is introduced into the system, it can lead to oxygen poisoning of the target.

**Table 4.1. Deposition rate data for aluminum oxide.**

| Sample Number | $O_2/(O_2+Ar)$ Percentage Ratio | Thickness (nm) | Rate (nm/s) |
|---|---|---|---|
| **1** | 0.00 | 107.16 | 0.262 |
| **2** | 4.76 | 80.98 | 0.198 |
| **3** | 9.09 | 78.94 | 0.193 |
| **4** | 13.04 | 65.03 | 0.159 |
| **5** | 16.67 | 54.81 | 0.134 |

Figure 4.1 depicts how the deposition rate changes when the oxygen flow is changed during the oxygen flow calibration for an aluminum metal target. The highest rate, 0.262 nm/s, occurred when there was no oxygen flow whereas the lowest rate, 0.134 nm/s, occurred when the highest flow of oxygen, 4 sccm, was used.

Iron reacted differently than aluminum to the introduction of oxygen into the system. When the oxygen to argon ratio was increased from 0 to 9, the deposition rate

actually increased from 0.089 nm/s to 0.106 nm/s. As the oxygen to argon ratio continued to increase however, the deposition rate began to decrease after the first initial spike. Figure 4.2 and Table 4.2 display the change in deposition rates of the iron samples as the oxygen to argon ratio changed.

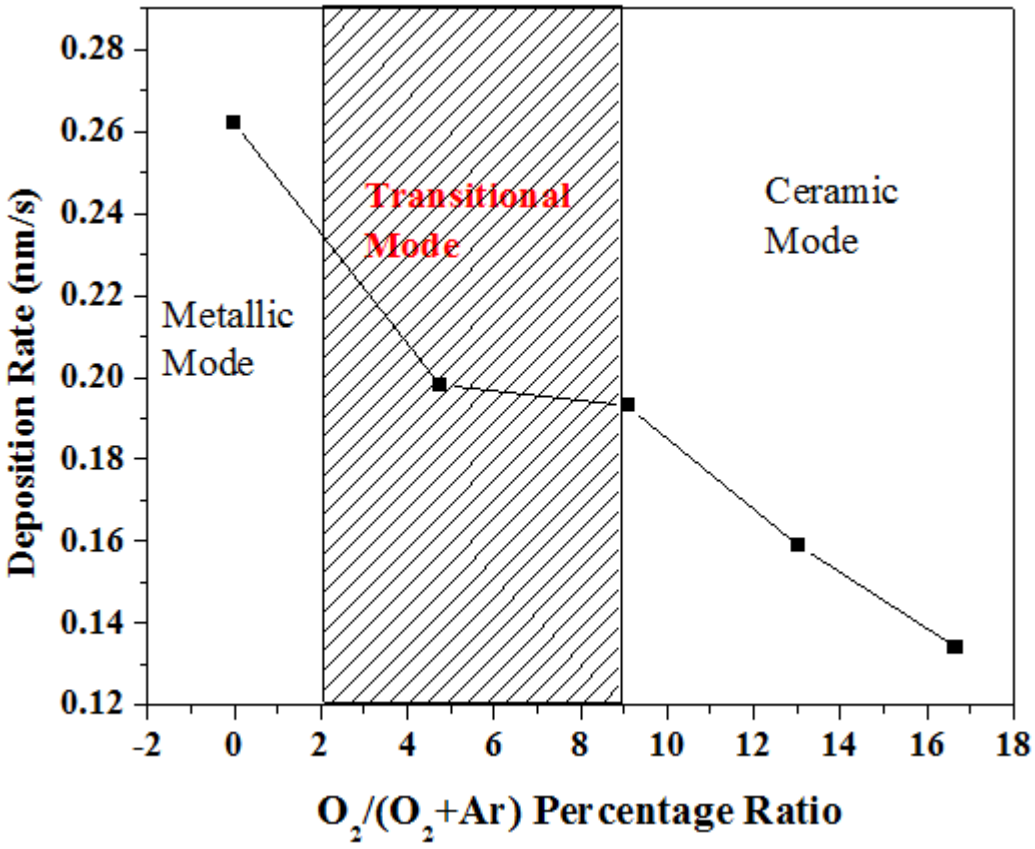


**Figure 4.1. Deposition rate versus $O_2/(O_2+Ar)$ percentage ratio for aluminum target.**

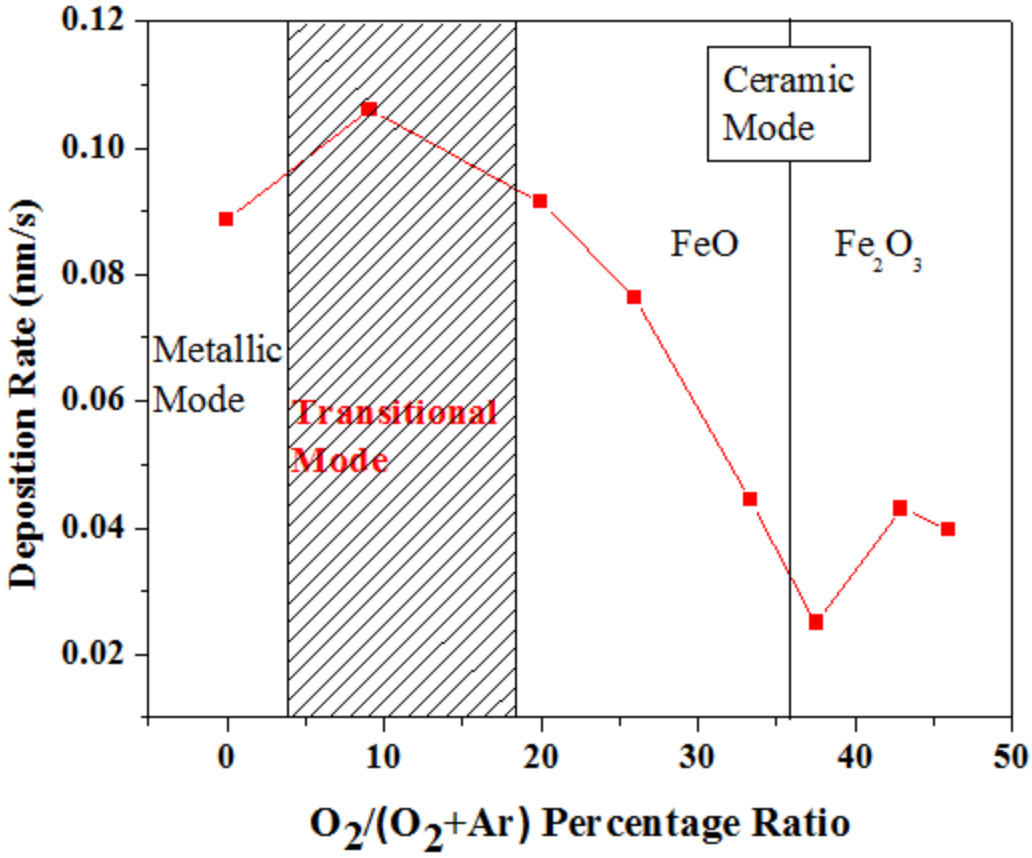


**Figure 4.2. Deposition rate versus $O_2/(O_2+Ar)$ percentage ratio for iron target.**

**Table 4.2. Deposition rate data for ferric oxide**

| Sample Number | $O_2/(O_2+Ar)$ Percentage Ratio | Thickness (nm) | Rate (nm/s) |
|---|---|---|---|
| **6** | 0.00 | 53.16 | 0.089 |
| **7** | 9.09 | 63.64 | 0.106 |
| **8** | 20.00 | 54.88 | 0.092 |
| **9** | 25.93 | 45.83 | 0.076 |
| **10** | 33.33 | 26.65 | 0.044 |
| **11** | 37.50 | 14.68 | 0.025 |
| **12** | 42.86 | 25.55 | 0.043 |
| **13** | 45.95 | 23.9 | 0.040 |

Zinc reacted in a similar manner compared to iron. Figure 4.3 shows how the deposition rate (nm/s) changed as the oxygen to argon ratio was increased. The highest deposition rate occurred with sample number 16, with a rate of 1.343 nm/s. The deposition rates of zinc also followed the same trend as those of iron. The rate increased as the oxygen to argon ratio increased from 0 to 6.25, and then began to decrease as the oxygen to argon ratio increased to 40. The deposition rate for each zinc oxide sample can be seen in Table 4.3.

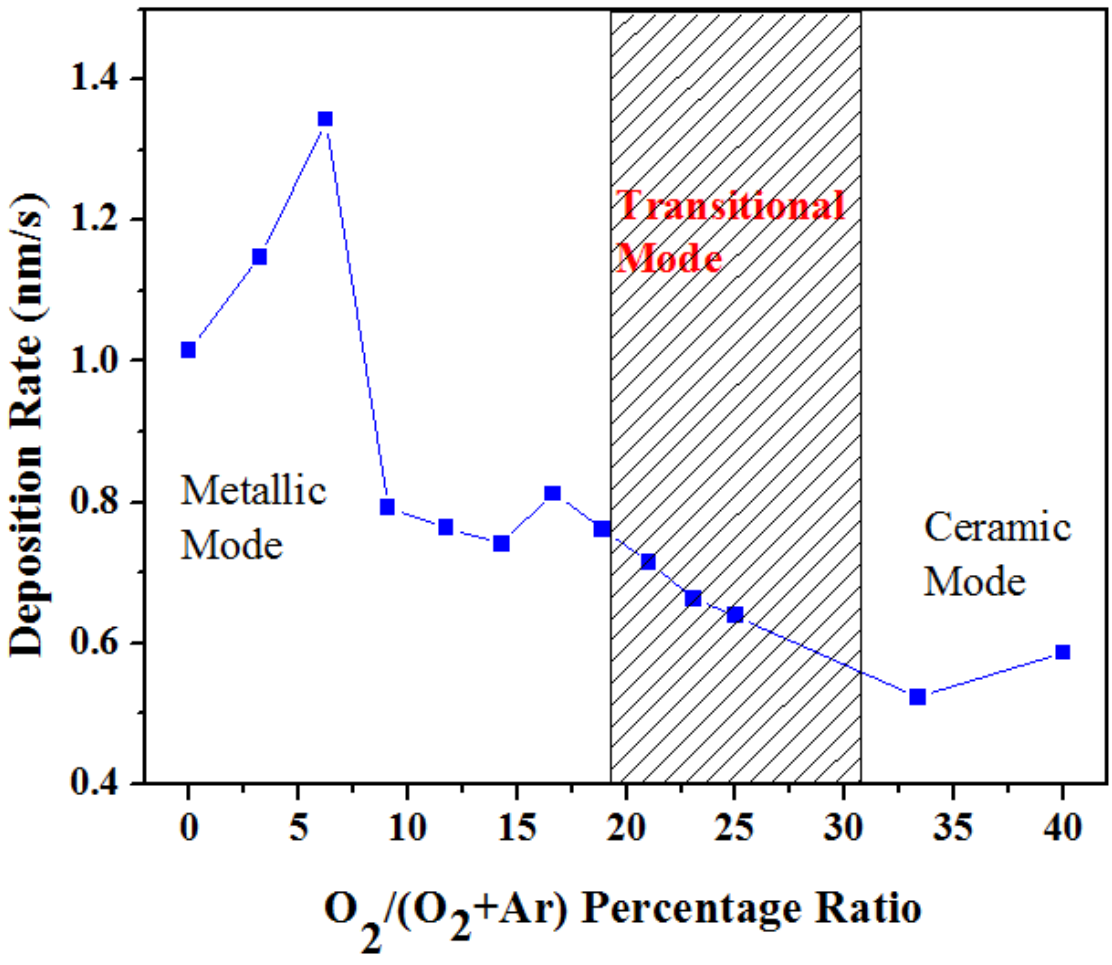


**Figure 4.3. Deposition rate versus $O_2/(O_2+Ar)$ percentage ratio for zinc target.**

**Table 4.3. Deposition rate data for zinc oxide.**

| Sample Number | $O_2/(O_2+Ar)$ Percentage Ratio | Thickness (nm) | Rate (nm/s) |
|---|---|---|---|
| **14** | 0.00 | 914.73 | 1.016 |
| **15** | 3.23 | 1033 | 1.148 |
| **16** | 6.25 | 1208.57 | 1.343 |
| **17** | 9.09 | 712.43 | 0.792 |
| **18** | 11.76 | 687.13 | 0.763 |
| **19** | 14.29 | 666.79 | 0.741 |
| **20** | 16.67 | 730.35 | 0.812 |
| **21** | 18.92 | 684.36 | 0.760 |
| **22** | 21.05 | 643.73 | 0.715 |
| **23** | 23.08 | 596.2 | 0.662 |
| **24** | 25.00 | 574.83 | 0.639 |
| **25** | 33.33 | 476.03 | 0.523 |
| 26 | 40.00 | 527.68 | 0.586 |

Although deposition rate was a critical factor in choosing which parameters would be used throughout the remainder of the study to manufacture each ceramic coating, the rates were not the only factor considered when deciding which sample of each ceramic would be used. After finding the rate, characterization of the samples was imperative to determine which samples would be used for biological testing.

## 4.2 Characterization

### *4.2.1 Optical Microscopy*

Upon completion of the oxygen flow calibration for the aluminum, iron and zinc targets, the resulting samples were measured for their transmittance of light resulting in Figure 4.4 and Equation (4.1):

$$2xMe + yO_2 \leftrightarrow 2Me_xO_y \tag{4.1}$$

where Me represents Al, Fe and Zn.

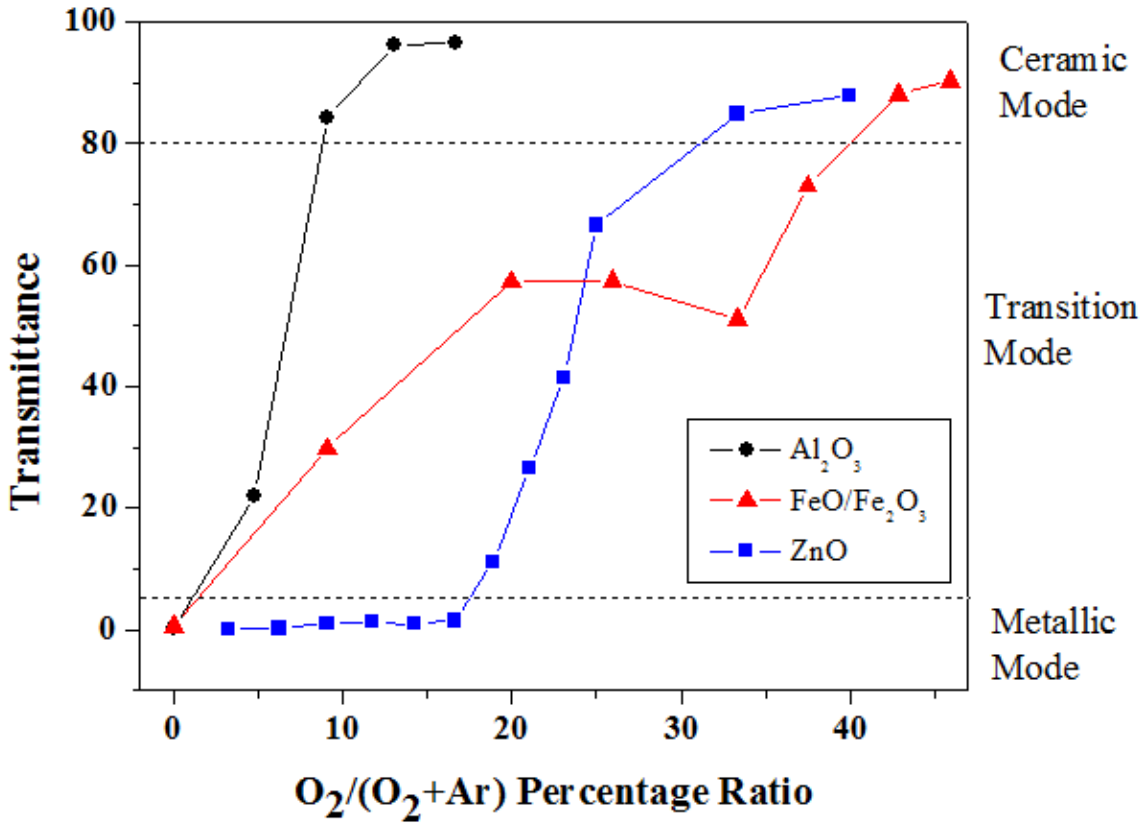


**Figure 4.4. Optical transmittance versus $O_2/(O_2+Ar)$ percentage ratio.**

As the samples transitioned from metal to ceramic, the transparency of the coating changed from opaque to transparent. From this, it was determined that aluminum, shown in red, was much more reactive than iron and zinc, therefore requiring less oxygen to produce a ceramic coating. As seen in Figure 4.4, the transmittance for aluminum and zinc have an ogive curve, resembling an "s," as was expected. Iron, however, has what appears to be a double ogive curve. This can be attributed to iron having two possible configurations in the ionic state. Iron can react with oxygen in two ways, shown below:

1) $2Fe + O_2 \rightarrow 2FeO$

2) $6Fe + 3O_2 \rightarrow 3Fe_2O_3$.

It is estimated that the form of iron oxide produced at ~25% oxygen to oxygen plus argon ratio, was ferrous oxide, FeO, while the iron oxide produced at ~45% oxygen to oxygen plus argon ratio was ferric oxide, $Fe_2O_3$.

The corrosion kinetics of the $Al_2O_3$ coatings were found from immersion tests using the optical density method. Figure 4.5 shows just a few images taken during the course of an immersion test. In Figure 4.5b, the magnesium has started to corrode due to the fluid coming through the pores of the $Al_2O_3$ coating.

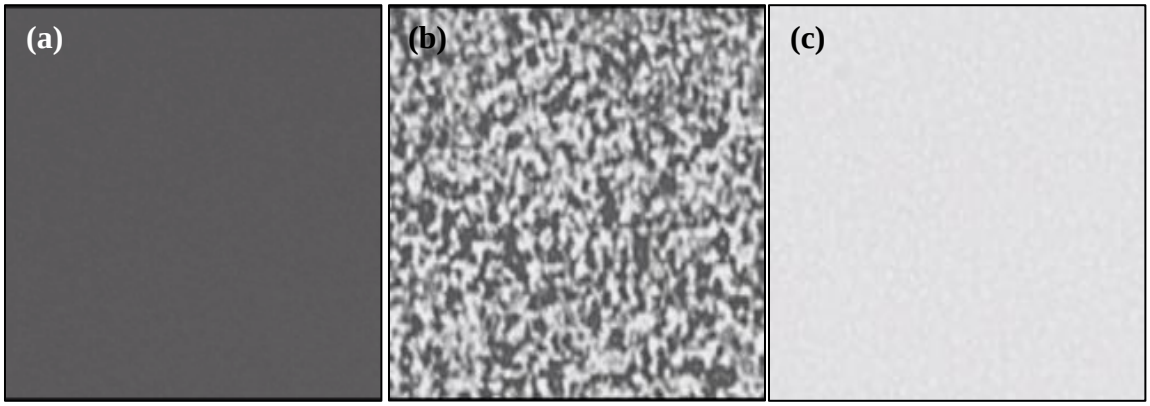


**Figure 4.5. (a) Image taken before sample was immersed. (b) Image taken during the middle of the immersion test. (c) Image taken at the end of immersion test.**

Figure 4.6, Figure 4.7 and Figure 4.8 show the corrosion kinetics of aluminum oxide obtained as a result of the immersion test. From Figure 4.6 it can be concluded that the 10 nm coating did not have pores that controlled the fluid flow, thus it was the quickest to corrode. As the thickness increased, the immersion time increased before the magnesium layer was completely degraded. Figure 4.7 depicts log porosity – log immersion time plot. In Figure 4.7, it can be seen that the log-log dependencies show constant slopes at

approximately 1% porosity. This indicates that the corrosion behavior of each thickness is uniform and it has been reported that if the corrosion process is uniform, the corrosion kinetics will also obey the power law, widely reported in the literature (Melchers 2003).

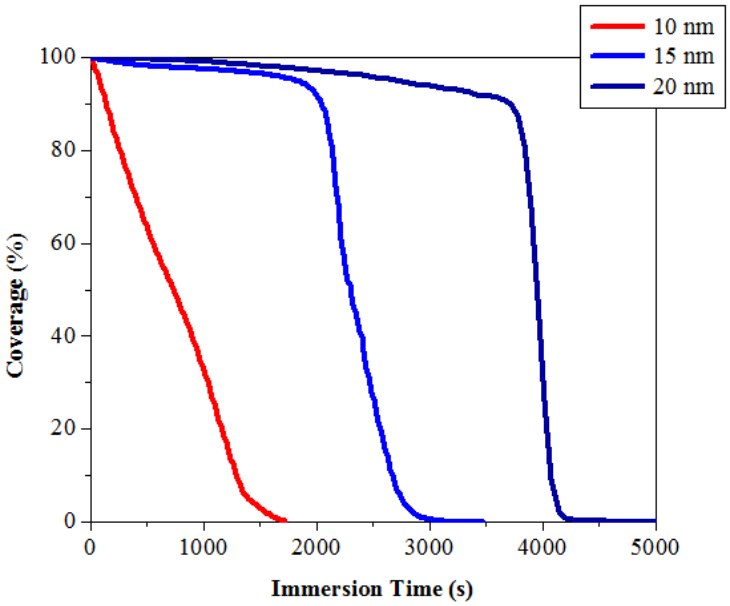


**Figure 4.6. Porosity versus immersion time.**

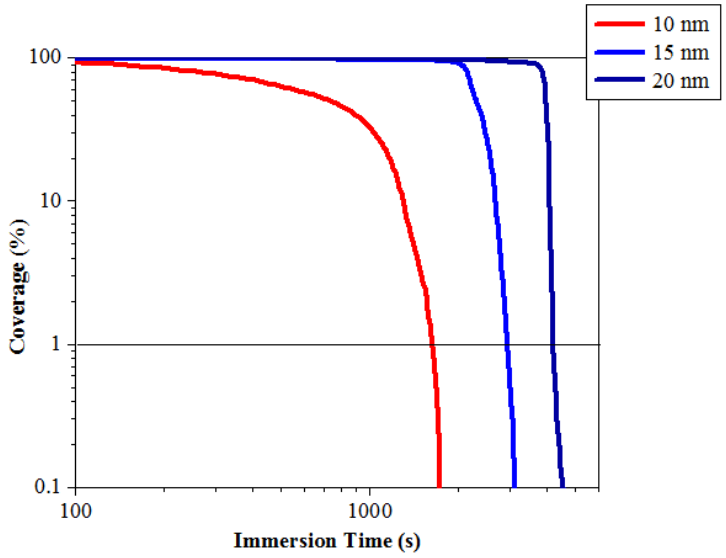


**Figure 4.7. Porosity versus immersion time in log, log scale.**

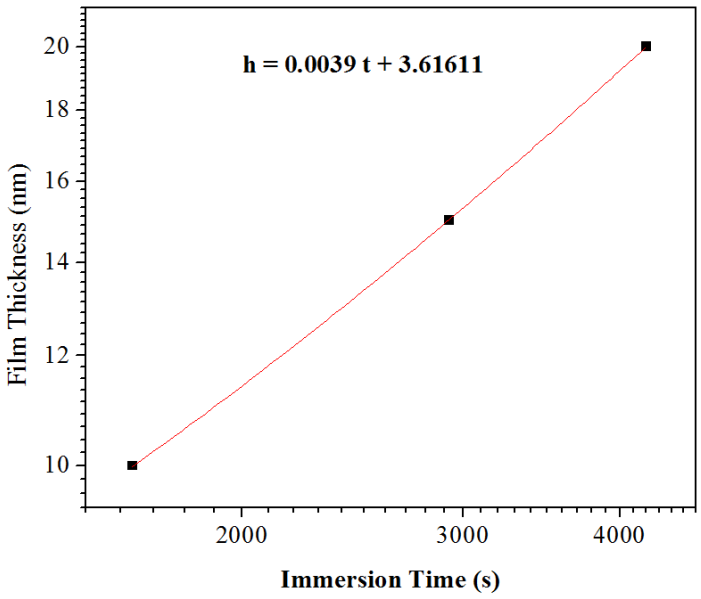


**Figure 4.8. Initial film thickness log (thickness) versus log *t* for residual thickness.**

Using these observations, for every film with initial thickness *h* (prior to immersion in corrosive medium), an immersion time $t_h$ can be obtained that is required for corrosion processes to reduce the film to its residual thickness (Kotoka, Yarmolenko et al. 2011). Due to this outcome, the film thickness could be compared to immersion time, shown in Figure 4.8. Table 4.4 contains the estimated thickness of $Al_2O_3$ coating needed to survive the given resorption time.

After determining the transmittance of each sample produced as part of the oxygen flow calibration, parameters to reproduce the ceramic coatings were chosen based on transmittance of the coating and deposition rate. Table 4.5 lists those parameters chosen to reproduce each coating for the duration of the study. For aluminum oxide coatings, the oxygen flow was 3 sccm with a deposition rate of 0.159 nm/s. For iron

oxide, the oxygen flow was 5 sccm with a deposition rate of 0.0915 nm/s. For zinc oxide, the oxygen flow was 10 sccm with a deposition rate of 0.639 nm/s.

**Table 4.4. $Al_2O_3$ film thickness required for different resorption times in 0.9 wt. % saline environment.**

| Resorption Time | Thickness (μm) |
|---|---|
| 1 h | 0.02 |
| 12 h | 0.17 |
| 1 day | 0.34 |
| 1 week | 2.36 |
| 1 month | 10.11 |
| 4 months | 40.44 |

**Table 4.5. Final deposition parameters used to reproduce coatings for the duration of the study.**

| Material | Working Pressure (mTorr) | Argon (sccm) | $O_2$ (sccm) | Time (s) | Thickness (nm) | Deposition Rate (nm/s) |
|---|---|---|---|---|---|---|
| Al | 2 | 20 | 3 | 409 | 65.03 | 0.159 |
| Fe | 2 | 20 | 5 | 600 | 54.90 | 0.0915 |
| Zn | 2 | 30 | 10 | 900 | 575.10 | 0.639 |

### *4.2.2 X-Ray Diffraction*

XRD patterns were found for each ceramic material, shown in Figure 4.9. The pattern for $Al_2O_3$ indicates that it has a monoclinic structure with lattice parameters, a = 11.795 Å, b = 2.91 Å and c = 5.64 Å. The pattern for $Fe_2O_3$ indicates a cubic structure with lattice parameter, a = 8.315 Å. The pattern for ZnO indicates a hexagonal structure with lattice parameters, a = 3.255 Å and c = 5.213 Å. Each pattern of the coating material corresponds to a pattern of the corresponding bulk materials meaning that magnetron

sputtering is capable of producing metal oxides by pulsed direct current sputtering method.

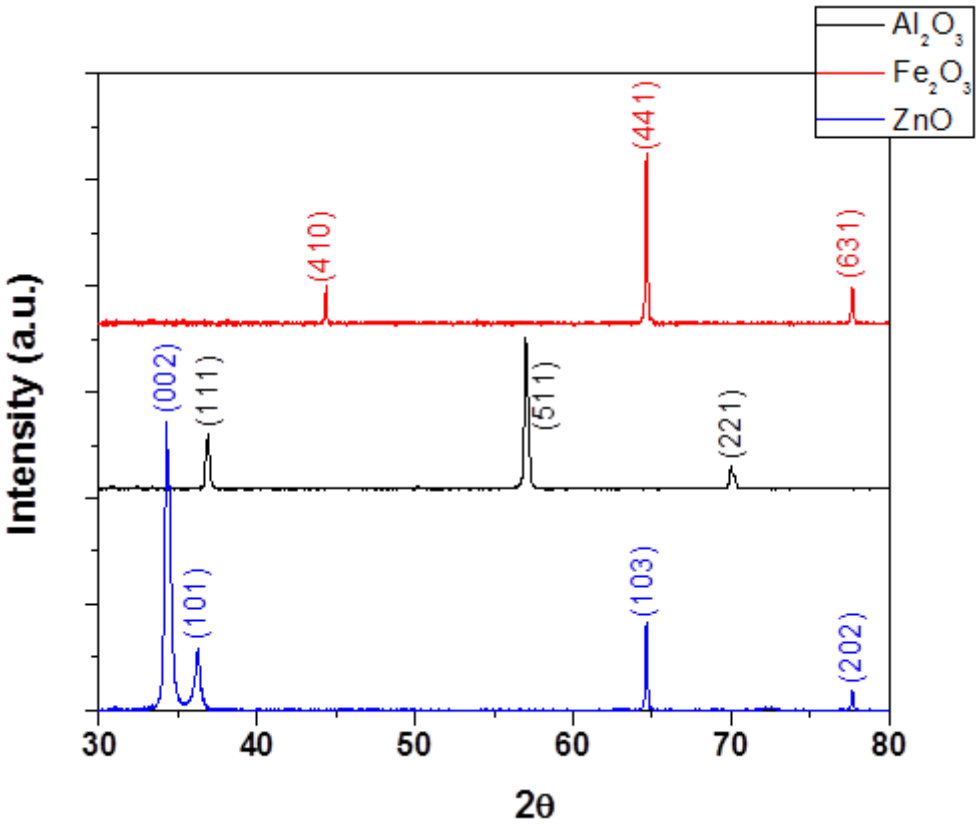


**Figure 4.9. XRD patterns of $Al_2O_3$ (black), $Fe_2O_3$ (red) and ZnO (blue).**

### *4.2.3 Scanning Electron Microscopy*

An image of each oxide coating was captured using a mixture of the SE and BSE detectors. These detectors focus on crystal orientation and surface information. The image of the aluminum oxide coating was captured over a time span of 80 s and at a magnification of 100,000. Figure 4.10 depicts the structure of the aluminum oxide coating. The coating was very smooth and was composed of very small grains. Figure

4.11 depicts the image of the iron oxide coating. The image of the iron oxide coating was captured over a time span of 80 s and at a magnification of 100k.

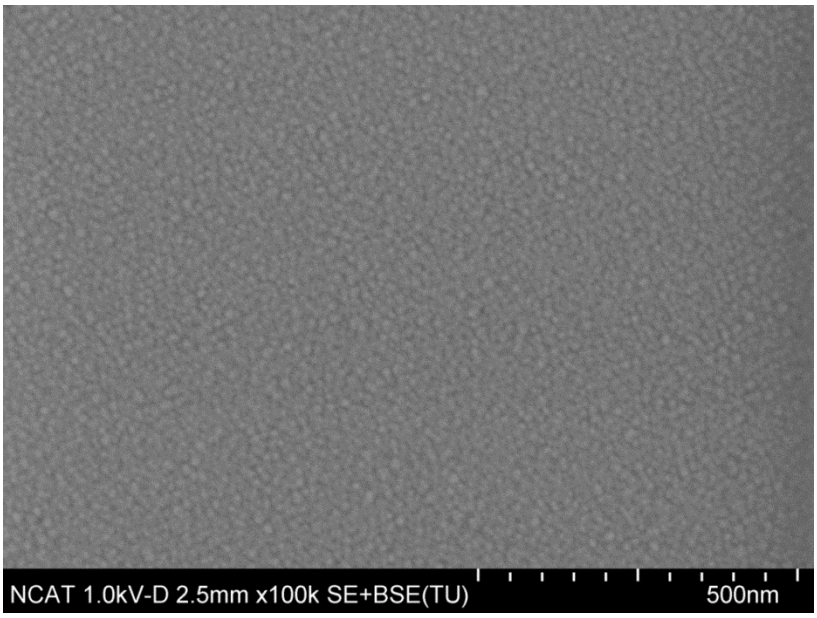


**Figure 4.10. Aluminum oxide coating.**

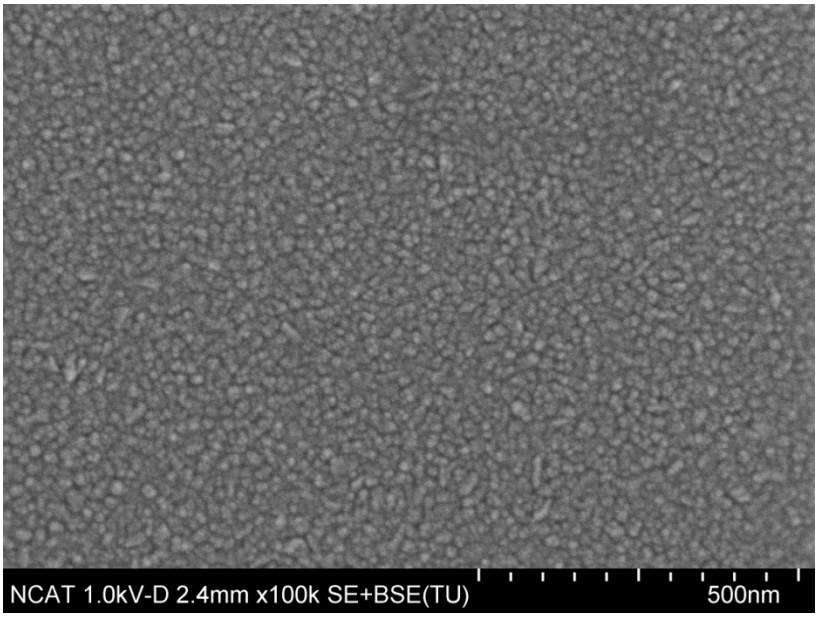


**Figure 4.11. Iron oxide coating.**

The grains of the iron oxide coating are bigger than those of the aluminum oxide coating. Due to the larger grain size, the pores of the iron oxide coating are also larger than those of the aluminum oxide coating. The zinc oxide coating, shown in Figure 4.12, had the largest grain size of the three ceramic coatings. The grains appear to be approximately 50 nm. Due to such large grain size, the zinc oxide coating had the largest pore size. The image of the zinc oxide coating was captured at a magnification of 100,000 over a time span of 40 s. The time span to capture the zinc oxide coating was shorter than those used to capture images of aluminum oxide and iron oxide due to charging.

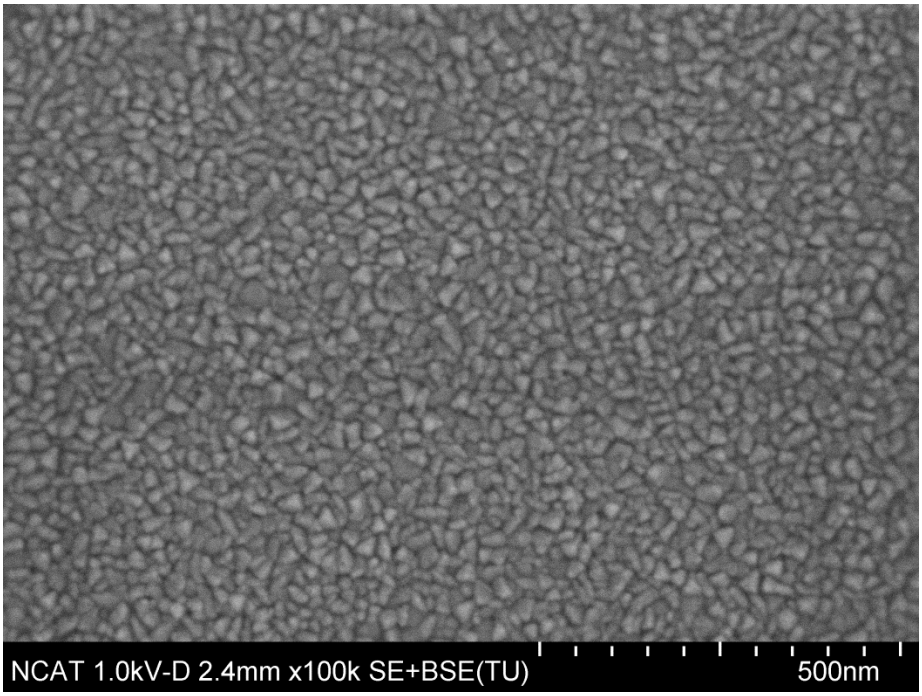


**Figure 4.12. Zinc oxide coating.**

### *4.2.4 Atomic Force Microscopy*

AFM was used to measure the surface roughness of 10 nm and 20 nm thick coatings of aluminum oxide, iron oxide and zinc oxide. Figure 4.13, depicts the resulting

images of the $Al_2O_3$ 10 nm and 20 nm coatings with a scan length of 500 nm. During image processing, the surface roughness was extracted and compiled into Table 4.6. The roughness of the 10 nm $Al_2O_3$ coating was 0.142 nm with a scan length of 500 nm and increased to 0.196 nm when the thickness increased to 20 nm. With a scan length of 1 µm, the surface roughness of the 10 nm $Al_2O_3$ coating as 0.157 nm and was 0.174 nm for the 20 nm $Al_2O_3$ coating. $Fe_2O_3$ and ZnO 10 nm and 20 nm coatings were also measured using both scan lengths: 500 nm and 1 µm, respectively. Figure 4.14 and Figure 4.15 show the AFM surface roughness images after the scans for $Fe_2O_3$ and ZnO, respectively. For the 500 nm scan length, the $Fe_2O_3$ 10 nm coating had a roughness of 0.263 nm, while the 20 nm coating had a roughness of 0.341 nm. The ZnO 10 nm coating had a roughness of 0.546 nm and the 20 nm ZnO coating had a roughness of 1.018 nm for the 500 nm scan length. For the 1 µm scan length, the 10 nm $Fe_2O_3$ coating had a surface roughness of 0.201 nm, while the 20 nm $Fe_2O_3$ coating had a roughness of 0.276 nm. The ZnO 10 nm coating had a roughness of 0.340 nm and the 20 nm ZnO coating had a surface roughness of 1.000 nm for the 1 µm scan length. Each coating's surface roughness increased as the thickness of the coating was increased from 10 nm to 20 nm.

Another finding was that the roughness decreased of the 10 nm coatings as the scan length was increased as shown in Figure 4.16. The decrease of surface roughness due to the increase of the scan length is due to sensitivity. With a scan length of 500 nm, the sensitivity of the instrument is increased, leading to a higher quality result compared to the result of a 1 µm scan length.

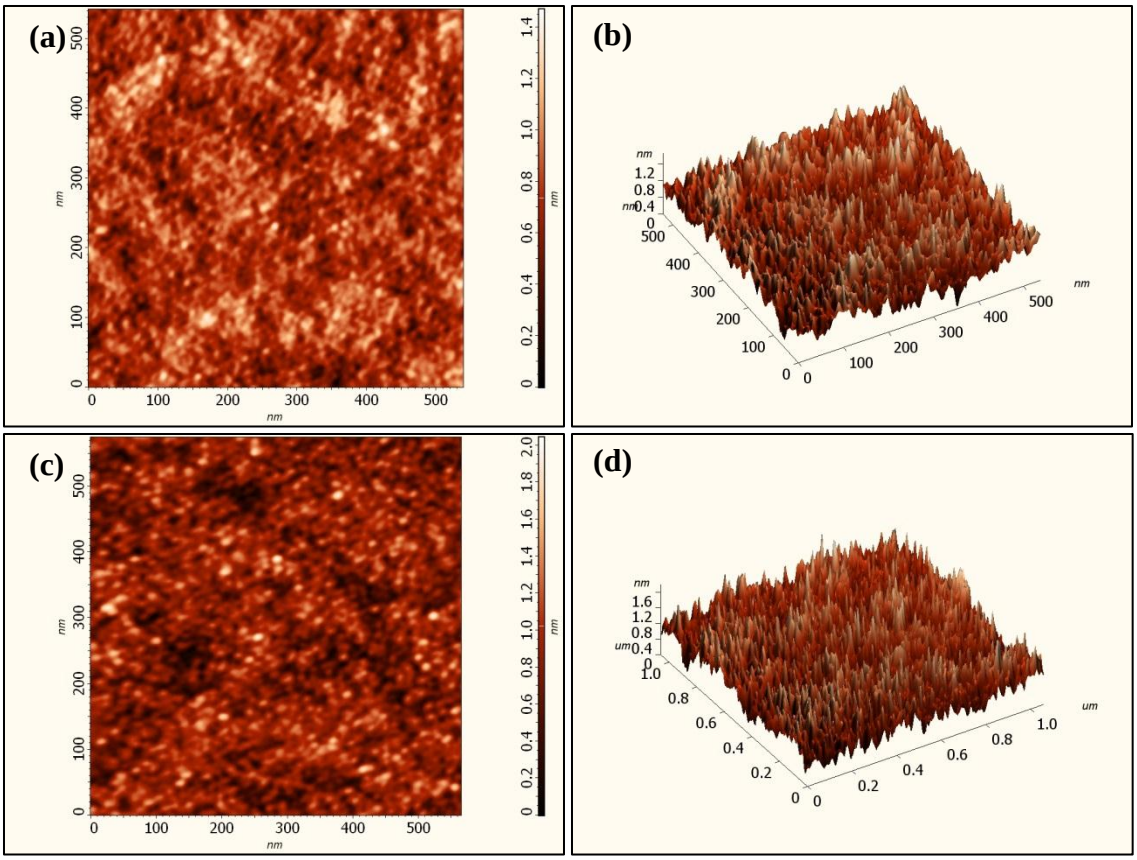


**Figure 4.13. AFM surface roughness of $Al_2O_3$. (a) and (b) 10 nm thick, 2D and 3D, respectively. (c) and (d) 20 nm thick, 2D and 3D, respectively.**

**Table 4.6. Surface roughness of aluminum oxide, iron oxide and zinc oxide 10 nm and 20 nm coatings.**

| **Sample Thickness** | **10 nm** | | **20 nm** | |
|---|---|---|---|---|
| **Material** | **Scan Length** | | **Scan Length** | |
| | 500 nm | 1 µm | 500 nm | 1 µm |
| **$Al_2O_3$** | 0.142 | 0.157 | 0.196 | 0.174 |
| **$Fe_2O_3$** | 0.263 | 0.201 | 0.341 | 0.276 |
| **ZnO** | 0.546 | 0.340 | 1.018 | 1.000 |

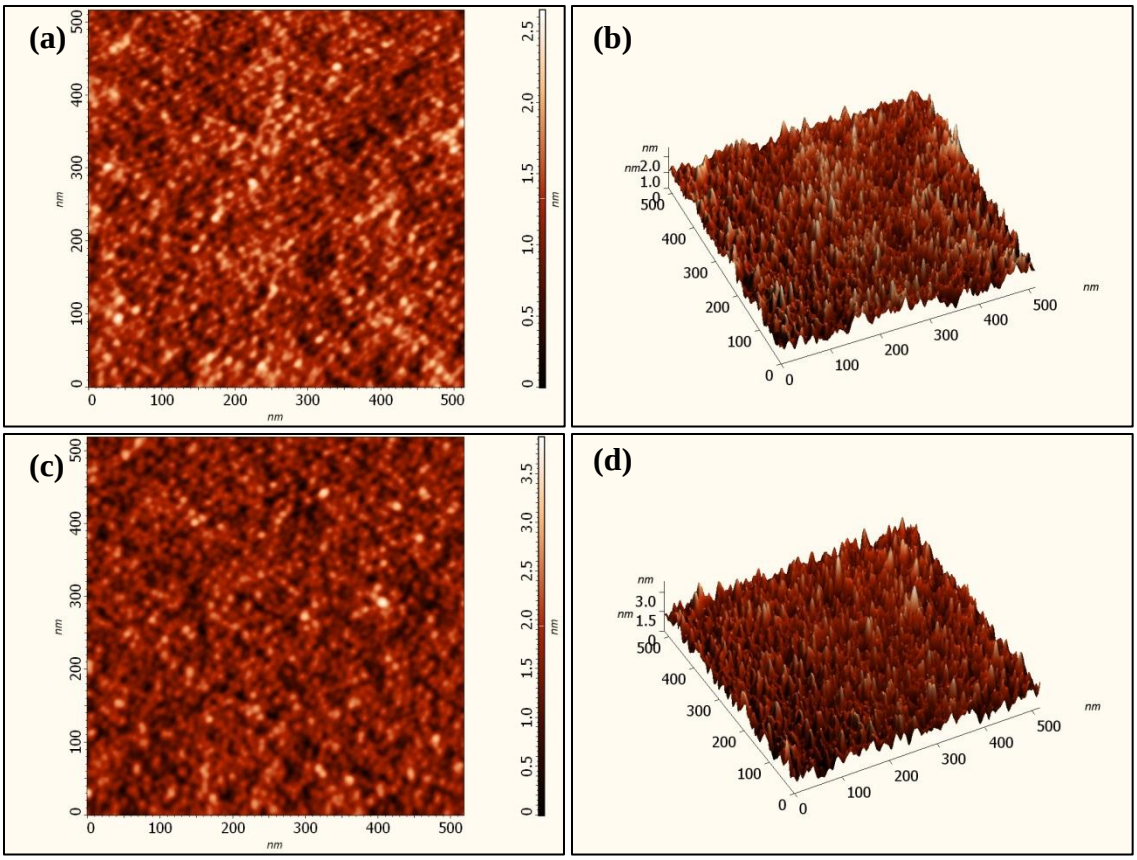


**Figure 4.14. AFM surface roughness of $Fe_2O_3$. (a) and (b) 10 nm thick, 2D and 3D, respectively. (c) and (d) 20 nm thick, 2D and 3D, respectively.**

### 4.3 Biological Adhesion Assay

Upon completion of the adhesion assay, a phase contrast image of each well of each plate was taken using an Advanced Microscopy Group EVOS-xl digital inverted microscope. When looking at the aluminum oxide plate, seen in Figure 4.17, the osteoblasts adhered to all substrates. Figure 4.17a shows the cells adhered to the blank well. The blank well acted as the control for the aluminum oxide plate. In this image, the cells adhered as well as began to grow processes. Figure 4.17b shows the cells adhered to the glass substrate. When capturing this image, it was noted that there appeared to be different layers of cells attached to the glass substrate. After further inspection, it was

determined that some of the cell/media suspension had leaked under the glass substrate and cells began to adhere to the well. The image was taken of the substrate. The leaking of media under the substrate applied to all wells with substrates in them, which accounts for what appears to be a blurry layer in the background of Figure 4.17b-e. Using visual inspection, there appears to be no difference in the attachment of the cells, as in each image the cells have adhered and began to spread processes.

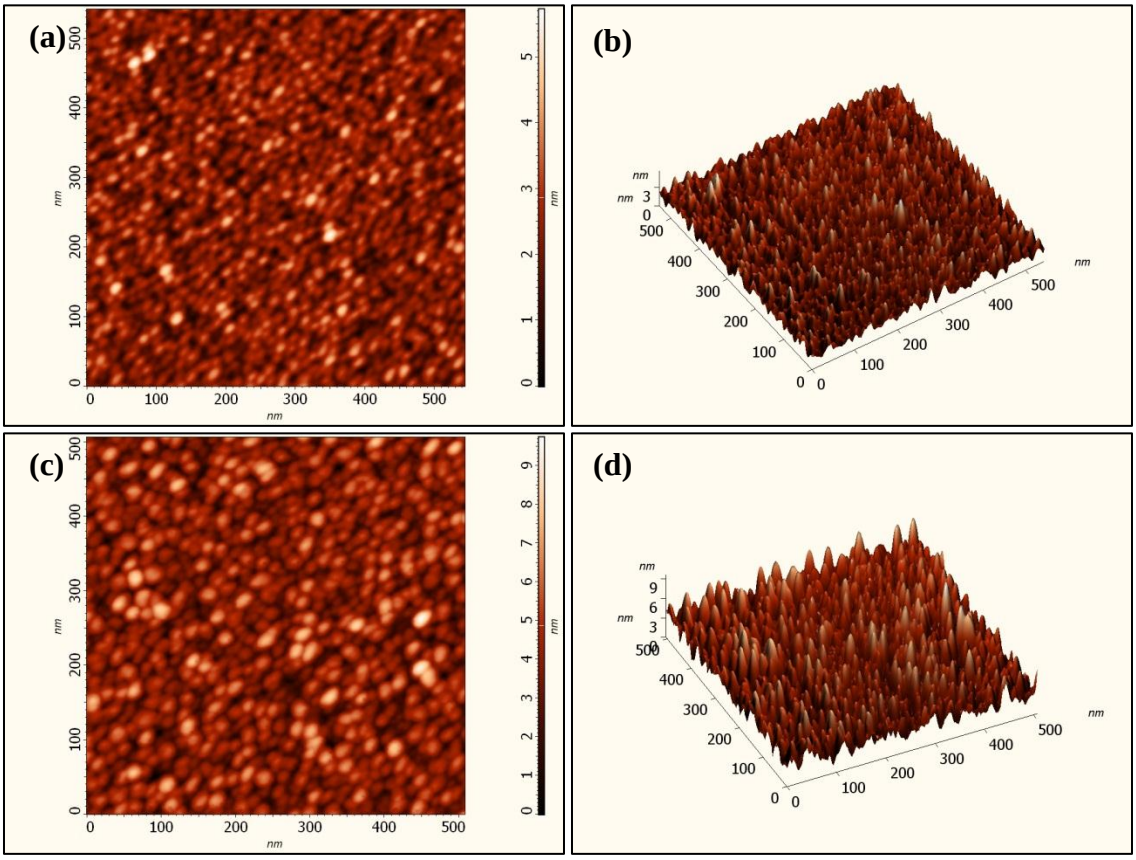


**Figure 4.15. AFM surface roughness of ZnO. (a) and (b) 10 nm thick, 2D and 3D, respectively. (c) and (d) 20 nm thick, 2D and 3D, respectively.**

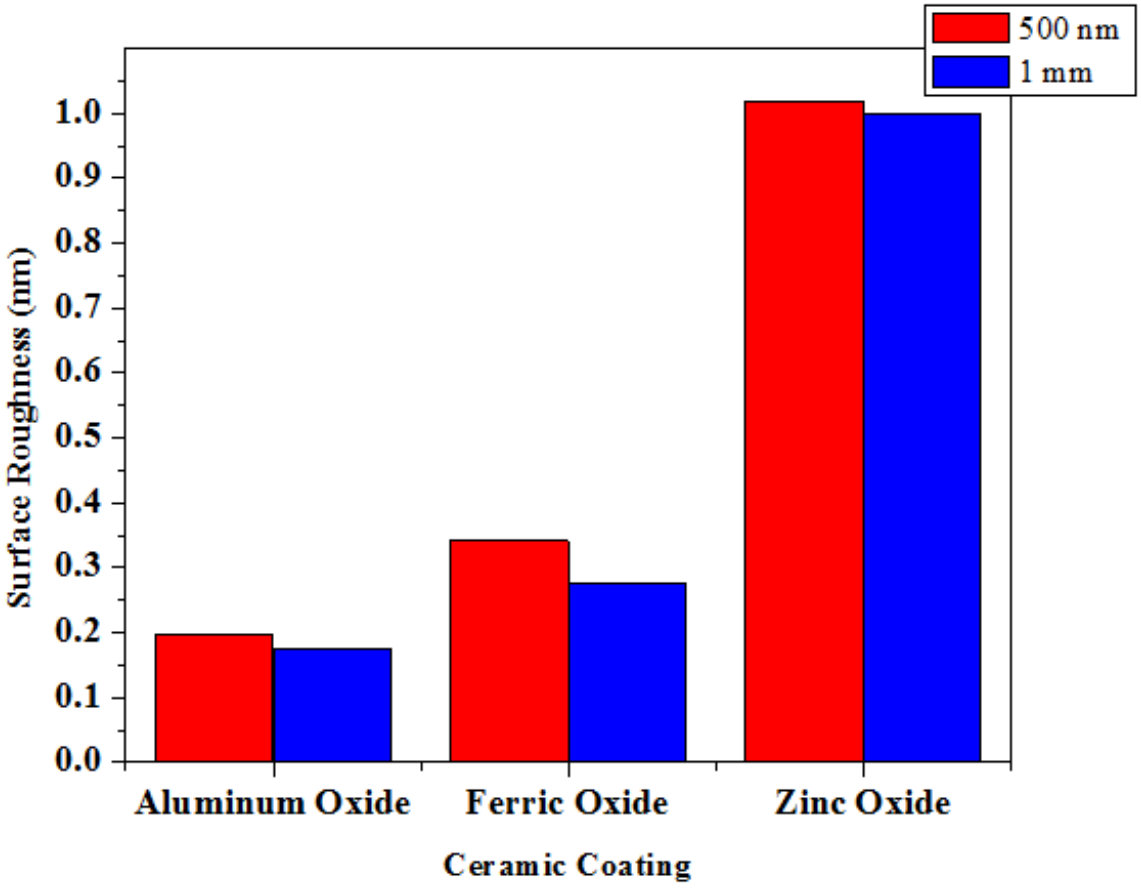


**Figure 4.16. Surface roughness of 20 nm ceramic coatings after both scan lengths: 500 nm and 1µm.**

An interesting finding when viewing the attachment of cells to the iron oxide coatings was that of coating delamination. Figure 4.18 images (d) and (e) show small portions of light seeping through the dark iron oxide coatings. Although the coating appears to be delaminating, the cells remain attached, indicating that the act of delamination caused no harm to the cells or was toxic to the cells in any way. The 150 nm iron oxide coating of Figure 4.18e had the most spots of light.

Although for the aluminum oxide and iron oxide coatings the cells attached and formed processes, the cells that attached to the zinc oxide coatings did not form processes

upon attachment. Figure 4.19 shows the progression of attachment where Figure 4.19a,b, the blank and glass substrate, show cell attachment with processes and Figure 4.19c-e show cells that have not laid down processes and have remained circular. The shape of the cells attached to the zinc oxide coating raise an alarm due to the characteristic of osteoblasts to exhibit an amorphic structure upon adhering to a surface. The fact that the cells have a spherical shape suggests that the cells are starting to detach from the surface. These cells were washed with PBS to ensure that the cells were attached.

Along with determining the adhesion of the cells to the ceramic coatings, the confluency of cells was estimated for the blank well, glass substrate, 100 nm aluminum oxide coating, 100 nm iron oxide coating and 100 nm zinc oxide coating. Figure 4.20 models the percent confluency of cells to each substrate. As seen, the confluency was higher for each of the coatings when compared to the blank well or glass substrate, thus the coatings were not toxic to the cells. Of the three ceramic coatings, ferric oxide exhibited the highest confluency with a mean of 85.83%. Due to the evidently preferential attachment of the cells to the coatings over the bare well and glass, a one-way analysis of the variance (ANOVA) was completed with Bonferroni post-test corrections to determine if there was a significant difference in the confluency of cells between the substrates. It was found that there was a highly significant difference in the means with a resulting P-value, $P < 0.0001$.

After using the ANOVA and Bonferroni's post-test corrections, the results were compiled into Table 4.7. The test comparing the bare well and glass substrate showed no statistical difference. From this result, it was determined that the glass substrate would be

used as the control, thus the confluency of each coating was compared to the confluency of the glass. There was a significant difference between the glass and all three coatings, but to various degrees. With $Al_2O_3$ compared to glass, the P-value was $P < 0.01$, indicated by "**" in the summary column of Table 4.7, while with $Fe_2O_3$ and ZnO compared to glass, the P-value was $P < 0.001$, indicated by "***" in the summary column of Table 4.7. The finding of a significant difference between the glass and the coatings indicates that the cells prefer the coatings. Another Bonferroni's test was completed to determine if the cells preferred one coating over the other two.

The results, shown in Table 4.7, indicate that there is a significant difference in confluency, i.e. cell attachment, between $Al_2O_3$ and $Fe_2O_3$ and $Al_2O_3$ and ZnO. Again the differences between the coatings varied. Between $Al_2O_3$ and $Fe_2O_3$, the P-value was $P < 0.001$, meaning that the cells preferred the $Fe_2O_3$ coating over the $Al_2O_3$ coating. Between $Al_2O_3$ and ZnO, the difference was not as significant with a resulting P-value of $P < 0.05$, indicating that the cells preferred the ZnO coating over the $Al_2O_3$ coating. When looking at the test results between the $Fe_2O_3$ coating and ZnO, there was no significant difference between the confluency of each.

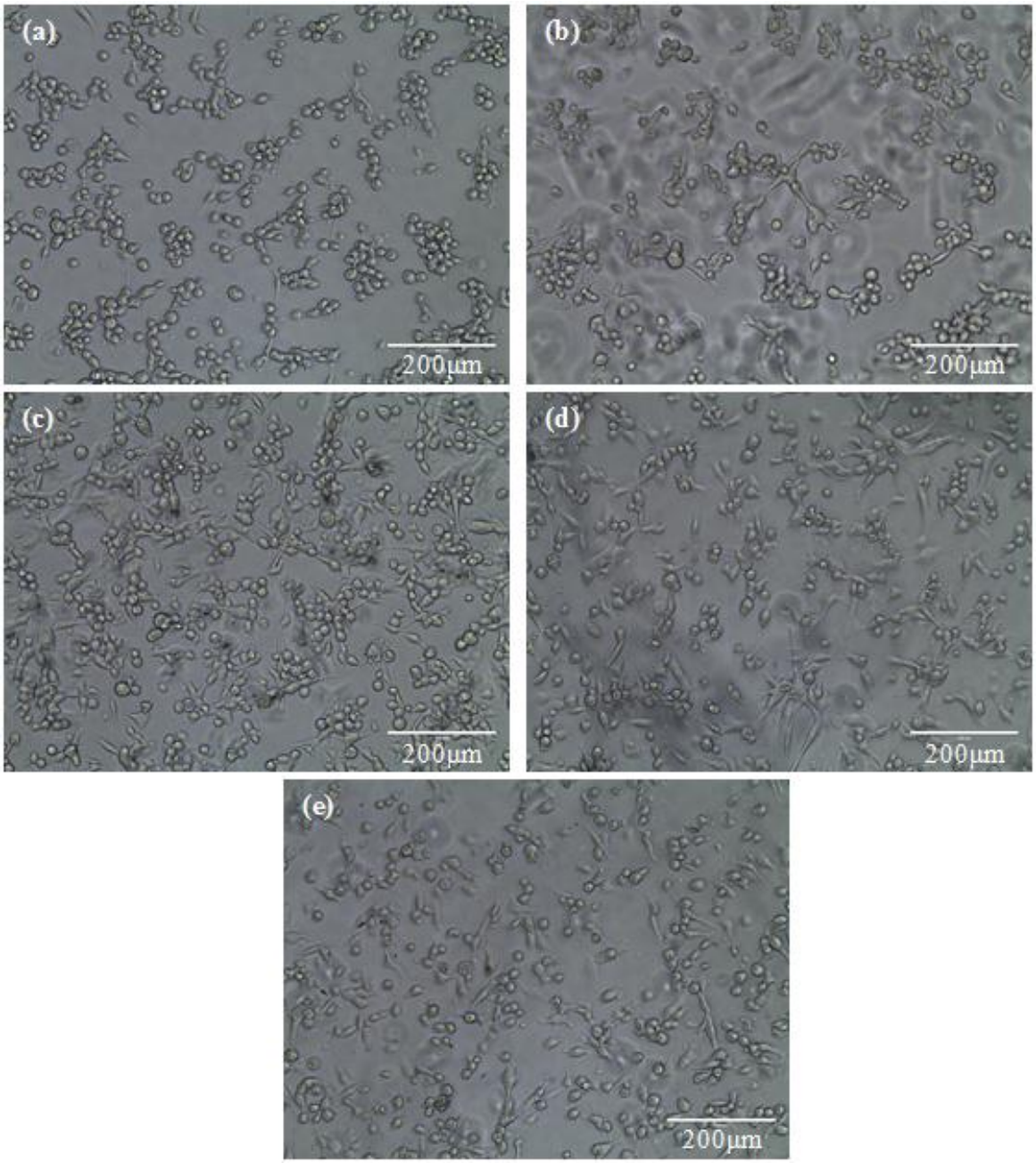


**Figure 4.17. Aluminum oxide adhesion assay results. (a) Blank well, (b) glass substrate, (c) 25 nm coating, (d) 50 nm coating and (e) 100 nm coating.**

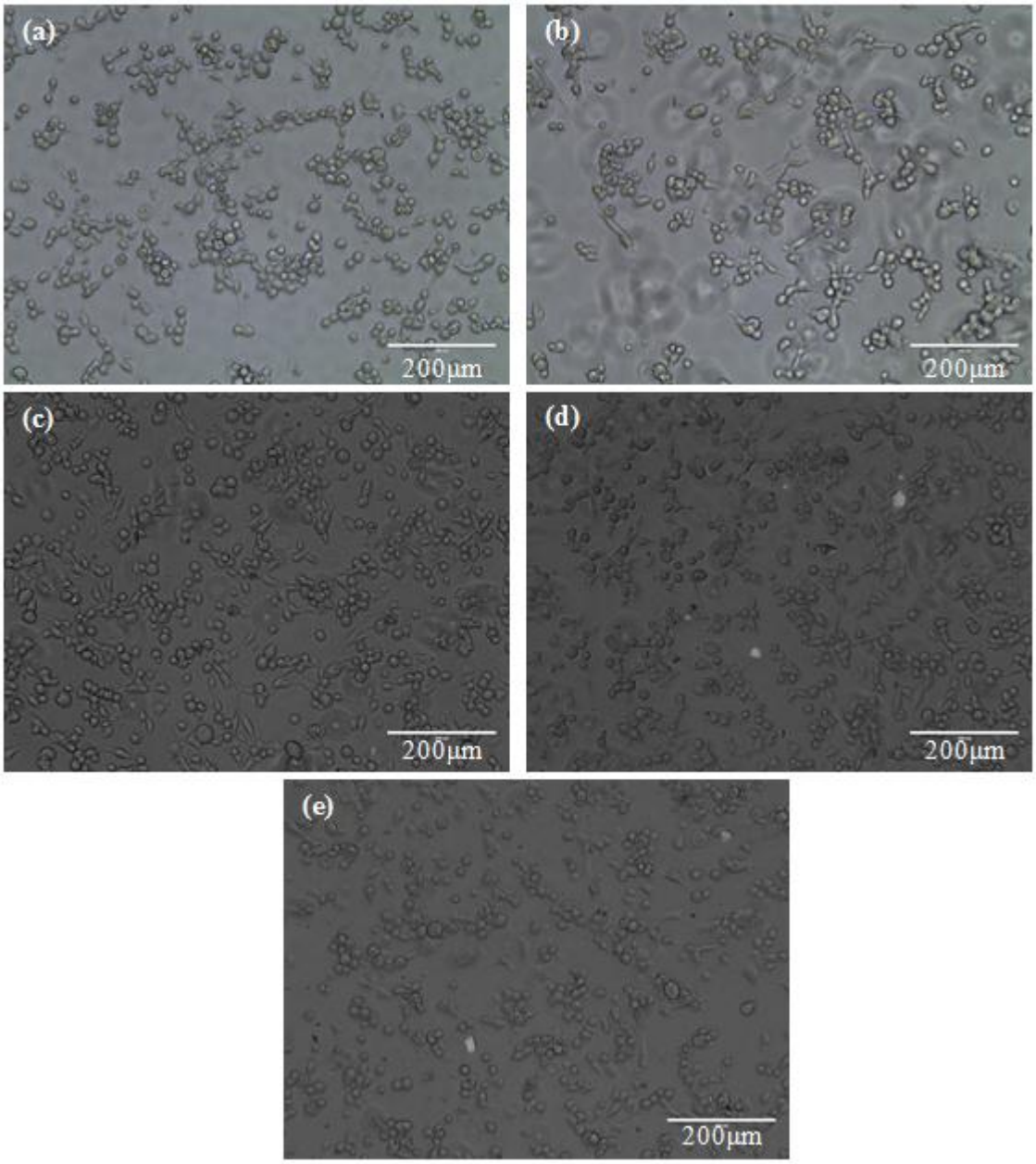


**Figure 4.18. Iron oxide adhesion assay results. (a) Blank well, (b) glass substrate, (c) 50 nm coating, (d) 100 nm coating and (e) 150 nm coating.**

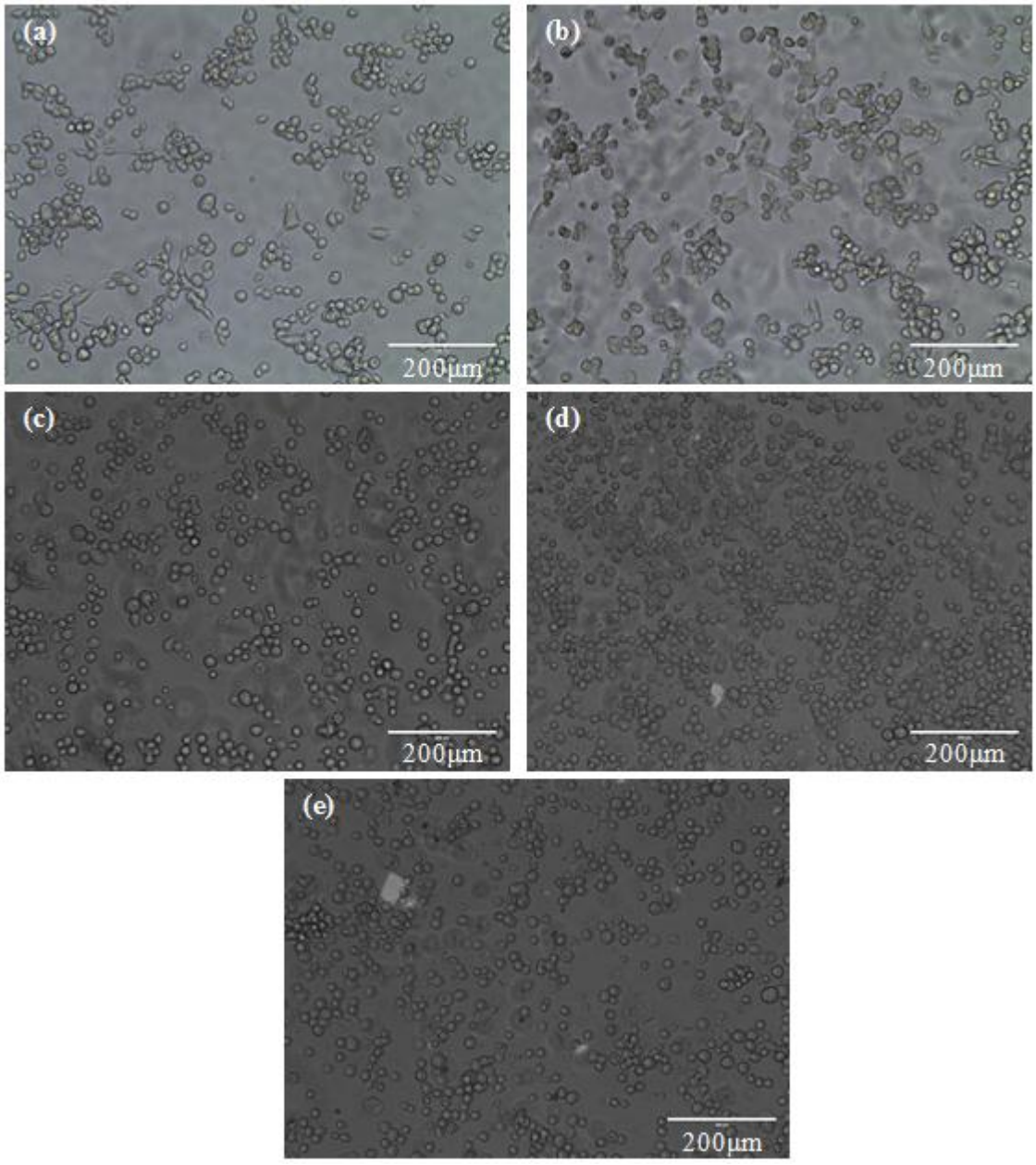


**Figure 4.19. Zinc oxide adhesion assay results. (a) Blank well, (b) glass substrate, (c) 50 nm coating, (d) 100 nm coating and (e) 150 nm coating.**

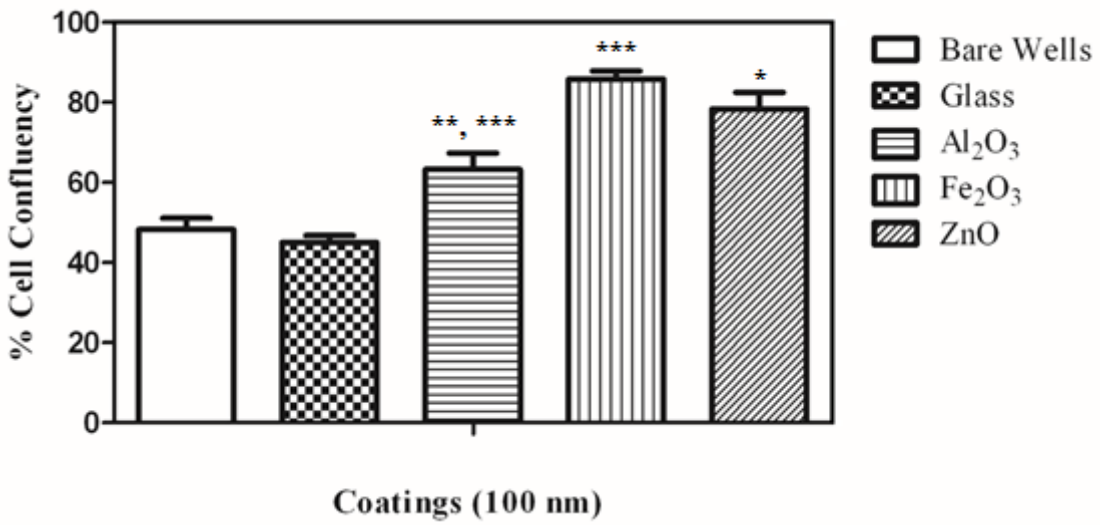


**Figure 4.20. Percent confluency of different substrates used in the adhesion assay.**

**Table 4.7. ANOVA statistical results of cell confluency.**

| Bonferroni's Multiple Comparison Test | Mean Diff. | t | Significant? P < 0.05? | Summary |
|---|---|---|---|---|
| **Bare Wells vs Glass** | 3.333 | 0.7527 | No | ns |
| **Glass vs $Al_2O_3$** | -18.33 | 4.14 | Yes | ** |
| **Glass vs $Fe_2O_3$** | -40.83 | 9.221 | Yes | *** |
| **Glass vs ZnO** | -33.33 | 7.527 | Yes | *** |
| **$Al_2O_3$ vs $Fe_2O_3$** | -22.5 | 5.081 | Yes | *** |
| **$Al_2O_3$ vs ZnO** | -15 | 3.387 | Yes | * |
| **$Fe_2O_3$ vs ZnO** | 7.5 | 1.694 | No | ns |

### 4.4 LIVE/DEAD Cell Viability Assay

The soaking test followed by the LIVE/DEAD assay provided an indirect way to measure the toxicity of the coatings. To determine whether the cells were alive or dead after being soaked with media from the soaking test, the 96-well plate was read using a fluorescence micro-plate reader. Live cells were distinguished by the presence of

ubiquitous intracellular esterase activity, determined by the enzymatic conversion of the virtually nonfluorescent cell-permeant calcein AM to the intensely fluorescent calcein. The polyanionic dye calcein AM was well retained within live cells, producing an intense uniform green fluorescence in live cells (ex/em ~495 nm/~515 nm). EthD-1 entered cells with damaged membranes and underwent a 40-fold enhancement of fluorescence upon binding to nucleic acids, thereby producing a bright red fluorescence in dead cells (ex/em ~495 nm/~635 nm). EthD-1 was excluded by the intact plasma membrane of live cells. The determination of cell viability depended on these physical and biochemical properties of cells. Background fluorescence levels are inherently low with this assay technique because the dyes are virtually non-fluorescent before interacting with cells (Inc. 2005). To determine the number of live cells, Equation (4.2) was utilized where: $F(530)_{sam}$ is the fluorescence at 530 nm in the experimental cell sample, labeled with calcein AM and EthD-1, $F(530)_{min}$ is the fluorescence at 530 nm in a sample where all (or nearly all) cells are alive, labeled with EthD-1 only, and $F(530)_{max}$ is the fluorescence at 530 nm in a sample where all (or nearly all) cells are alive, labeled with calcein AM only.

$$\%\ Live\ Cells = \frac{F(530)_{sam} - F(530)_{min}}{F(530)_{max} - F(530)_{min}} * 100\% \qquad (4.2)$$

After completing the LIVE/DEAD assay, statistical analysis was performed on the number of live cells for each sample at each concentration. Figure 4.21 and Figure 4.22 model the percent cell viability for 100 nm coatings after the one day and three day soaking experiments, respectively. From both Figure 4.21 and Figure 4.22, it can be seen that the cell viability does not follow the dose response that was expected. Usually as the concentration of the “toxic” material, used media in this study, is increased, the cell

viability will decrease. In both the one-day and three-day soaking experiments, a decrease in cell viability is seen up to the 5% concentration and then the viability increases at the 12.5% concentration. In the one day soaking experiment, a significant difference was found between the glass and $Al_2O_3$ cell viability at the 5% concentration. As stated, this response was not expected, thus requires further investigation.

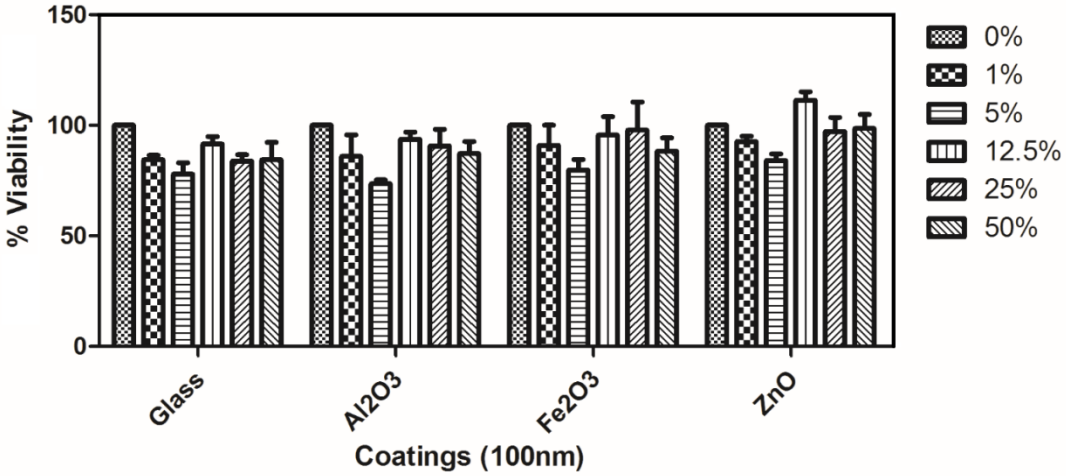


**Figure 4.21. Percent cell viability per control for 100 nm coatings after one-day soaking experiment.**

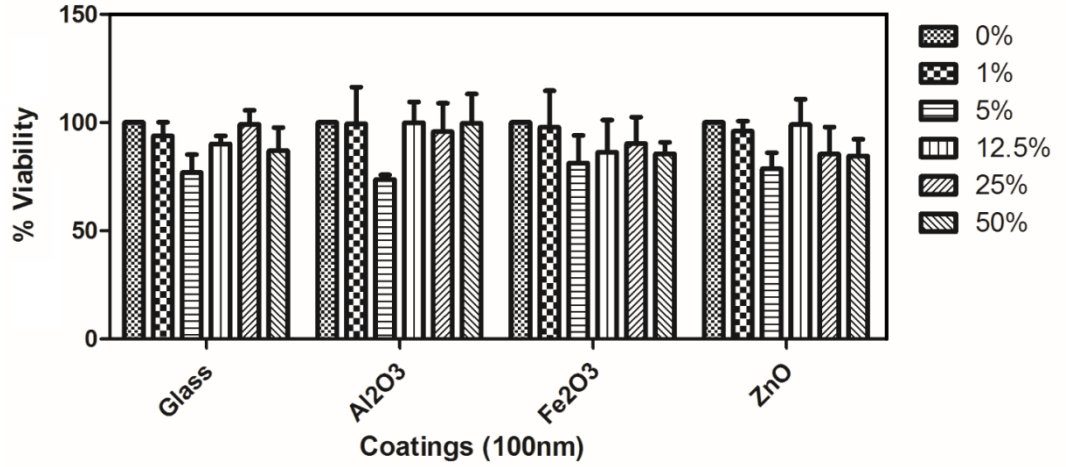


**Figure 4.22. Percent cell viability per control for 100 nm coatings after three-day soaking experiment.**

# CHAPTER 5

# CONCLUSIONS

Magnetron sputtering was used to manufacture high quality ceramic coatings through the PDC technique. These ceramic coatings were characterized by the optical density method, XRD, SEM and AFM. The optical density method was used to determine the transparency of the ceramic coatings after an oxygen flow calibration as well the corrosion kinetics of $Al_2O_3$ in a 0.9 percent wt. saline solution. XRD was used to ensure the ceramic coating patterns corresponded to the bulk material patterns. SEM images were used to analyze the porosity of the coating. After characterization, the ceramic coatings were tested for their biocompatibility by a cell adhesion assay as well as with a LIVE/DEAD assay. From this study it was found that:

1) The magnetron sputtering system at NCAT can produce high quality oxide coatings using the PDC technique.
2) An optical density method can be used to obtain resorption rates of coatings. This method can also be used to predict the resorption time of coating of known thickness and consequently help to predict the thickness of a coating based on its resorption time.
3) A cell adhesion assay was completed to determine if human osteoblasts would attach to the ceramic coatings. Samples with thicknesses of 25 nm, 50 nm and 100 nm of $Al_2O_3$ along with samples with thicknesses of 50 nm, 100 nm and 150 nm of $Fe_2O_3$ and ZnO were seeded with osteoblasts and incubated for four hours. After incubation, images were taken of the cells attached to the coatings. The percent of cell confluency

was estimated and these values were used to complete a one-way ANOVA test to determine if there was a significant difference between the confluency of each coating. From the results of the ANOVA test, it can be concluded that osteoblast cells prefer to adhere to $Al_2O_3$, $Fe_2O_3$ and ZnO coatings over a bare well of a 96-well plate or a glass substrate. Of the three coatings, there was a significant difference between the confluency of $Al_2O_3$ compared to $Fe_2O_3$ and ZnO. The confluency of $Fe_2O_3$ and ZnO showed no significant difference, however, it can be concluded that the cells preferred the $Fe_2O_3$ coating over the ZnO coating based on the cell morphology. The cells had an amorphic structure when attached to $Fe_2O_3$, which is characteristic of osteoblasts when they attach to a surface, whereas on the ZnO coating, the cells appeared to be spherical in shape, which indicates the cells were beginning to detach from the coating. The $Al_2O_3$, $Fe_2O_3$ and ZnO coatings fabricated were determined to be biocompatible based upon the cell attachment to each coating.

4) Preliminary protocols for a LIVE/DEAD cell viability assay were developed. Samples of 100 nm thickness of each ceramic were soaked for one day and three days and then the soaked media was added to fresh media. A concentration gradient ranging from 0% to 50% soaked to fresh media was used to soak osteoblast cells in a 96-well plate for one day. After the soaking period, the 96-well plate was read using a fluorescence micro-plate reader. The percentage of cell viability per percent control was found. A dose response was not seen in either the one-day or three-day soaking test. The biocompatibility of the coatings based upon findings from the LIVE/DEAD cell viability assay could not be determined. For future tests, a larger range of

concentrations should be used to determine the effects of the soaked media on the cells.

5) $Al_2O_3$, $Fe_2O_3$ and ZnO were chosen as galvanic separator materials for the new generation of magnesium-based metallic implants because of their biocompatibility.

Future work will include studies on other slower degrading biocompatible oxides such as $ZrO_2$ and bioglass as galvanic separators between the magnesium-based implant and a functional coating. In continuing studies of $Al_2O_3$, $Fe_2O_3$ and ZnO, it will be important to obtain corrosion kinetics for $Fe_2O_3$ and ZnO as well evaluate mechanical properties such as adhesion, hardness, abrasive properties and shear strength for all three materials in multilayered coatings. It will be important to determine the biocompatibility of the coatings on bulk magnesium and its alloys as well as to determine different biological assays suitable for implant applications using multilayered metal/metal oxide coatings. From this study, $Al_2O_3$, $Fe_2O_3$ and ZnO were proven to be good galvanic separator materials as well as biocompatible. Using ceramic materials as intermediate layers between magnesium-based implants and functional metallic coatings has the ability to create many applications for the use of magnesium implants.

# REFERENCES


AAC Ltd. (2010). "What is Galvanic Corrosion?" Retrieved April 26, 2012, from http://aluminium.org.au/FAQRetrieve.aspx?ID=43870.

Ahluwalia, H. (2012). "Cracked: The Secrets of Stress Corrosion Cracking." Retrieved 5/5/12, from http://csidesigns.com/flowgeeks/cracked-the-secrets-of-stress-corrosion-cracking/.

Altun, H. and S. Sen (2006). "The Effect of PVD Coatings on the Corrosion Behaviour of AZ91 Magnesium Alloy." Materials & Design **27**(10): 1174-1179.

Basu, B., N. Saha, et al. (2010). "Sintering, Microstructure, Mechanical, and Antimicrobial Properties of HAp-ZnO Biocomposites." Journal of Biomedical Materials Research Part B-Applied Biomaterials **95B**(2): 430-440.

Belkind, A., A. Freilich, et al. (2005). "Characterization of Pulsed DC Magnetron Sputtering Plasmas." New Journal of Physics **7**.

Bruker. (2012). "X-Ray Diffraction." Retrieved 4/26/12, from http://www.bruker-axs.com/x_ray_diffraction.html.

Ceralink, I. (2008). "Structural Ceramics." Retrieved 5/15/12, from http://www.ceralink.com/structural.htm.

Chim, H. and A. K. Gosain (2009). "Biomaterials in Craniofacial Surgery: Experimental Studies and Clinical Application." Journal of Craniofacial Surgery **20**(1): 29-33 10.1097/SCS.1090b1013e318190dd318199e.

Choudhary, L. and R. K. S. Raman (2012). "Magnesium Alloys as Body Implants: Fracture Mechanism Under Dynamic and Static Loadings in a Physiological Environment." Acta Biomaterialia **8**(2): 916-923.

Corrosionist. (2012). "Galvanic Corrosion Bimetallic Corrosion." Retrieved 4/26/12, from http://www.corrosionist.com/Galvanic_Corrosion.htm.

Cottis, R. A. (2012). Guides to Good Practice in Corrosion Control: Stress Corrosion Cracking, National Physical Laboratory, UK**:** 16.

Dang, W. L., Y. Q. Fu, et al. (2007). "Deposition and Characterization of Sputtered ZnO Films." Superlattices and Microstructures **42**(1-6): 89-93.

De, R., N. Perugini, et al. (2001). "Degradation of Zinc Oxide Thin Films in Aqueous Environment: Part I - Bare Films." Mater. Corros. **52**(Copyright (C) 2011 American Chemical Society (ACS). All Rights Reserved.): 844-852.

Delaunay, C., I. Petit, et al. (2010). "Metal-on-Metal Bearings Total Hip Arthroplasty: The Cobalt and Chromium Ions Release Concern." Orthopaedics & Traumatology-Surgery & Research **96**(8): 894-904.

FDA. (2012). "Information for Orthopaedic Surgeons about Metal-on-Metal Hip Implant Surgery." Retrieved 5/12/12, from http://www.fda.gov/MedicalDevices/ProductsandMedicalProcedures/ImplantsandProsthetics/MetalonMetalHipImplants/ucm241667.htm.

Fewster, P. F. (1996). "X-Ray Analysis of Thin Films and Multilayers." Reports on Progress in Physics **59**(11): 1339-1407.

Frei, M. (2011). "Cell Viability and Proliferation." Retrieved 5/7/12, from http://www.sigmaaldrich.com/technical-documents/articles/biofiles/cell-viability-and-proliferation.html.

Ginsburg, E. (2002). "Sputtering." Retrieved 5/9/12, from www.eng.tau.ac.il/~yosish/courses/vlsi/Sputtering1.ppt.

Glassman, A. H., J. D. Bobyn, et al. (2006). "New Femoral Designs - Do They Influence Stress Shielding?" Clinical Orthopaedics and Related Research(453): 64-74.

Gradwell, S. (2010). "A Brief History of Dental Implants." Retrieved 4/24/12, from http://www.lehighvalleyperiodontist.com/a-brief-history-of-implants.html.

Gray, J. E. and B. Luan (2002). "Protective Coatings on Magnesium and Its Alloys - A Critical Review." Journal of Alloys and Compounds **336**(1-2): 88-113.

Grove, T. C. (2000). Arcing Problems Encountered During Sputter Deposition of Aluminum. A. Energy. Fort Collins, Colorado, Advanced Energy**:** 1.

Hazer, D. B., E. Kılıçay, et al. (2012). "Poly(3-hydroxyalkanoate)s: Diversification and Biomedical Applications." Materials Science and Engineering: C **32**(4): 637-647.

Hickman, K. (1999). "Bioceramics." Retrieved 5/15/12, from http://www.csa.com/discoveryguides/archives/bceramics.php.

Hitachi (2012). SU8000 Detector System: Variety of Signal Detection System. North Carolina, Hitachi**:** 1.

Jacobs, J. J., N. J. Hallab, et al. (2003). "Metal Degradation Products - A Cause for Concern in Metal-on-Metal Bearings?" Clinical Orthopaedics and Related Research(417): 139-147.

Jacobs, J. J., A. K. Skipor, et al. (2004). "Can Metal Levels Be Used to Monitor Metal-on-Metal Hip Arthroplasties?" Journal of Arthroplasty **19**(8): 59-65.

Karriem-Norwood, V. (2012). "Understanding Bone Fractures." Retrieved 4/24/12, from http://www.webmd.com/a-to-z-guides/understanding-fractures-basic-information.

Kelly, P. J., P. S. Henderson, et al. (2000). "Reactive Pulsed Magnetron Sputtering Process for Alumina Films." Journal of Vacuum Science & Technology a-Vacuum Surfaces and Films **18**(6): 2890-2896.

Kotoka, R., S. Yarmolenko, et al. (2011). Novel Application of Optical Density Technique to Evaluation of Corrosion Behavior of Metallic Thin Films. ASME 2011 International Mechanical Engineering Congress & Exposition. Denver, Colorado.

K.T. Corporation (2010). Alpha-Step IQ. K.-T. Corporation. Milpitas, CA, KLA - Tencor Corporation: 1-2.

Mattox, D. M. (2010). Handbook of Physical Vapor Deposition (PVD) Processing. Kidlington, Oxford, UK, Elsevier.

Melchers, R. E. (2003). "Mathematical Modelling of the Diffusion Controlled Phase in Marine Immersion Corrosion of Mild Steel." Corrosion Science **45**(5): 923-940.

Metallurgical Technologies, I. (2012). Stress Corrosion Cracking. I. S. C. Cracking. Mooresville, NC, Metallurgical Technologies, Inc. .

Miller, W. K. (1993). "Stress-corrosion Cracking." ASM: 251.

Morley, N. "Radio-Frequency (RF) Magnetron Sputtering." Retrieved 5/7/12, 2012, from http://dspace.jorum.ac.uk/xmlui/handle/123456789/15353?show=full.

M.P. Inc. (2005). LIVE/DEAD Viability/Cytotoxicity Kit for Mammalian Cells. Eugene, OR, Molecular Probes Inc.**:** 1-7.

Musil, J., P. Baroch, et al. (2005). "Reactive Magnetron Sputtering of Thin Films: Present Status and Trends." Thin Solid Films **475**(1-2): 208-218.

Nita, T. (2011). "Concepts in Biological Analysis of Resorbable Materials in Oro-Maxillofacial Surgery." Revista de Chirurgie Oro-Maxilo-Facială şi Implantologie: 33-38.

NT-MDT. (2012). "Semicontact Mode." Retrieved 5/4/12, from http://www.ntmdt.com/spm-principles/view/afm.

Pettersen, S. H., T. S. Wik, et al. (2011). "Subject Specific Finite Element Analysis of Stress Shielding Around a Cementless Femoral Stem (vol 24, pg 196, 2009)." Clinical Biomechanics **26**(4): 429-429.

Rice, P. (2012). "Charging Effects on SEM Images." Retrieved 5/9/12, from http://ncf.colorado.edu/instdocs/quickguides/SEM-ChargingEffects.pdf.

Saris, N. E. L., E. Mervaala, et al. (2000). "Magnesium - An Update on Physiological, Clinical and Analytical Aspects." Clinica Chimica Acta **294**(1-2): 1-26.

Sharma, S. K., N. Sehgal, et al. (2003). "Biomolecules for development of biosensors and their applications." Current Applied Physics **3**(2-3): 307-316.

Skar, J. I. (1999). "Corrosion and Corrosion Prevention of Magnesium Alloys." Materials and Corrosion-Werkstoffe Und Korrosion **50**(1): 2-6.

Song, G. L. and A. Atrens (1999). "Corrosion Mechanisms of Magnesium Alloys." Advanced Engineering Materials **1**(1): 11-33.

Southern California Orthopedic Institute (2012). "Revision ACL Considerations." Retrieved 5/12/12, from http://www.scoi.com/revision-acl.htm.

Sproul, W. D., D. J. Christie, et al. (2005). "Control of Reactive Sputtering Processes." Thin Solid Films **491**(1-2): 1-17.

Staiger, M. P., A. M. Pietak, et al. (2006). "Magnesium and Its Alloys as Orthopedic Biomaterials: A Review." Biomaterials **27**(9): 1728-1734.

Tresco, P. A. (2006). "Metals." Retrieved 5/23/12, from http://www.bioen.utah.edu/faculty/PAT/Courses/biomaterials2006/Metals%20and%20Applications%20in%20Orthopedics.pdf.

Wasa, K., Hayakawa, S. (1992). Handbook of Sputter Deposition Technology. Westwood, NJ, Noyes Publications.

Wikipedia. (2012). "Pitting Corrosion." Retrieved 5/9/12, from http://en.wikipedia.org/wiki/Pitting_corrosion.

Wikipedia. (2012). "Sputter Deposition." Retrieved 5/7/12, from http://en.wikipedia.org/wiki/Sputter_deposition.

Winzer, N., A. Atrens, et al. (2005). "A Critical Review of the Stress Corrosion Cracking (SCC) of Magnesium Alloys." Advanced Engineering Materials **7**(8): 659-693.

Wu, G. S., X. Q. Zeng, et al. (2006). "Preparation and Characterization of Ceramic/Metal Duplex Coatings Deposited on AZ31 Magnesium Alloy by Multi-Magnetron Sputtering." Materials Letters **60**(5): 674-678.

Zberg, B., P. J. Uggowitzer, et al. (2009). "MgZnCa Glasses Without Clinically Observable Hydrogen Evolution for Biodegradable Implants." Nature Materials **8**(11): 887-891.

Zeng, R. C., J. Zhang, et al. (2006). "Review of Studies on Corrosion of Magnesium Alloys." Transactions of Nonferrous Metals Society of China **16**: S763-S771.